A STUDY OF FLOW AND TEMPERATURE DISTRIBUTION AROUND A SINGLE CHANNEL IN CANDU MODERATOR

A STUDY OF FLOW AND TEMPERATURE DISTRIBUTION AROUND A SINGLE CHANNEL IN CANDU MODERATOR

BY

AZIN BEHDADI, B.Sc.

A THESIS

SUBMITTED TO THE DEPARTMENT OF ENGINEERING PHYSICS

AND THE SCHOOL OF GRADUATE STUDIES

OF MCMASTER UNIVERSITY

IN PARTIAL FULFILMENT OF THE REQUIREMENTS

FOR THE DEGREE OF

MASTER OF APPLIED SCIENCE

Master of Applied Science (2009) McMaster University

(Engineering Physics) Hamilton, Ontario, Canada

TITLE:	A STUDY OF FLOW AND TEMPERATURE DISTRIBUTION AROUND A SINGLE CHANNEL IN CANDU MODERATOR
AUTHOR:	Azin Behdadi B.Sc., (Chemical Engineering) Arak University, Arak, Iran
SUPERVISOR:	Prof. Luxat
NUMBER OF PAGES:	xiv, 104

Abstract

A 2D computational fluid dynamics (CFD) model has been developed to calculate the moderator velocity field and temperature distribution around a single channel inside the moderator of a CANDU reactor after a postulated ballooning deformation of the pressure tube (PT) into contact with the calandria tube (CT). Following contact between the hot PT and the relatively cold CT, there is a spike in heat flux to the moderator surrounding the CT which may lead to sustained CT dryout. This can detrimentally affect channel integrity if the CT post-dryout temperature becomes sufficiently high to result in thermal creep strain deformation. The present research is focused on establishing the limits for dryout occurrence on the CTs for the situation in which pressure tube-calandria tube contact occurs. In order to consider different flow patterns inside the calandria, both upward and downward flow directions have been analyzed for buoyancy dominant and momentum dominant flows respectively. The standard $k-\varepsilon$ and also $k-\omega$ turbulence models associated with logarithmic wall function are applied independently to predict the effects of turbulence and the results have been compared. The governing equations are solved by the finite element software package COMSOL. The buoyancy driven natural convection on the outer surface of a CT has been analyzed to predict the flow and temperature distribution around the single CT considering the local moderator subcooling, wall temperature

and heat flux. According to the flow pattern and temperature distribution, it is predicted that stable film boiling generates in the stagnation region on the cylinder and it has been compared with the related experimental data.

Acknowledgements

I would like to express the deepest appreciation to my supervisor Dr. John C. Luxat for his encouragement, guidance and support throughout my graduate studies. I would also like to thank Dr. David Novog for his advance thermalhydraulic course which was really helpful for me to find the way through my research. The financial support of the Natural Science and Engineering Research Council (NSERC) and the University Network of Excellence in Nuclear Engineering (UNENE) is gratefully acknowledged. I would like to thank my colleagues in JHE 327 room for their discussion and friendship.

I am deeply indebted to my parents for their support in every aspect of my life. My special gratitude is due to my sister and my brothers for their loving support. Last but not least, I would like to give my special thanks to my husband Farshad for his unlimited help and endurance. His perpetual encouragement and patient love enabled me to complete this work.

Notation and Abbreviations

A	Surface area
C_p	Specific heat at constant pressure
D	Characteristic length
F_x	x-component of external forces
F_y	y-component of external forces
H	Enthalpy
L	Arc-length
Nu	Nusselt number
Pr	prandtl number
Pr_T	Turbulent prandtl number
Q	Heat source
T	Temperature
$\bar{\mathbf{u}}$	Mean component of turbulent velocity
β	Thermal expansion coefficient
δ_w	Wall offset
δ	Boundary layer thickness
$\dot{E}_g$	The rate at which thermal energy may be generated due to conversion from other energy forms

$\dot{E}_{in}$	Thermal and mechanical energy enter the control volume through the control surface
$\dot{E}_{out}$	Thermal and mechanical energy leave the control volume through the control surface
$\dot{E}_{st}$	Rate of energy stored in the control volume
$\dot{q}$	Energy generated rate per unit volume
ϵ	Dissipation rate of turbulent
$\hat{\mathbf{n}}$	Outward unit normal to the surface
κ	Von Karman constant
$\mu\Phi$	Viscous dissipation
μ	Dynamic viscosity
μ_T	Turbulent eddy viscosity
∇	Vector differential operator
ν	Kinematic viscosity
ω	Dissipation per unit turbulent kinetic energy
ρ	Density
σ	Normal stress
τ	Shear stress
τ_w	Wall shear stress
$\mathbf{F}$	External force
$\mathbf{F}_s$	Internal forces
$\mathbf{u}$	Velocity in a two dimensional system,$\mathbf{u} = u\hat{i} + v\hat{j}$
$\mathbf{u}'$	Fluctuating component of turbulent velocity
k	Thermal conductivity

e	Internal energy
h	Convection heat transfer coefficient
k	Turbulent kinetic energy
k_T	Turbulence thermal conductivity
l^*	Viscous lengthscale
p	Pressure
q''	Heat flux
t	Time
u	Velocity in x-direction
u_∞	Free stream velocity
u_τ	Velocity at the wall
v	Velocity in y-direction
CANDU	CANada Deuterium Uraniium
CFD	Computational Fluid Dynamics
CHF	Critical Heat Flux
CT	Calandria Tube
DOF	Degree Of Freedom
FEM	Finite Element Method
IST	Industry Standard Toolset
LOCA	Loss Of Coolant Accident
PDE	Partial Differential Equation
PT	Pressure tube

Contents

List of Figures

Chapter 1

Introduction and Problem Statement

In this thesis, we investigate the flow and temperature distribution around one single channel inside the moderator of the CANada Deuterium Uranium Pressurized Heavy Water (CANDU-PHW) reactor in normal conditions and also after a postulated accident in which the pressure tube (PT) contacts to its calandria tube (CT). In this introductory chapter, we comment the reasons to establish this investigation. Included in the first section is the concept of moderator as a heat sink in CANDU reactors, followed by the aspects of a critical break LOCA in CANDU reactors. Subsequently, the literature pertinent to the moderator flow and temperature is reviewed followed by a brief introduction to finite element method.

1.1 Moderator Heat Sink

In a CANDU reactor, the calandria is a horizontal cylindrical tank, filled by heavy water moderator circulated by a system of pumps at a rate of about $1m^3/s$. This vessel is 6 m long and its diameter is about 7.6 m. Figure 1.1 shows the simplified geometry of the CANDU calandria vessel.

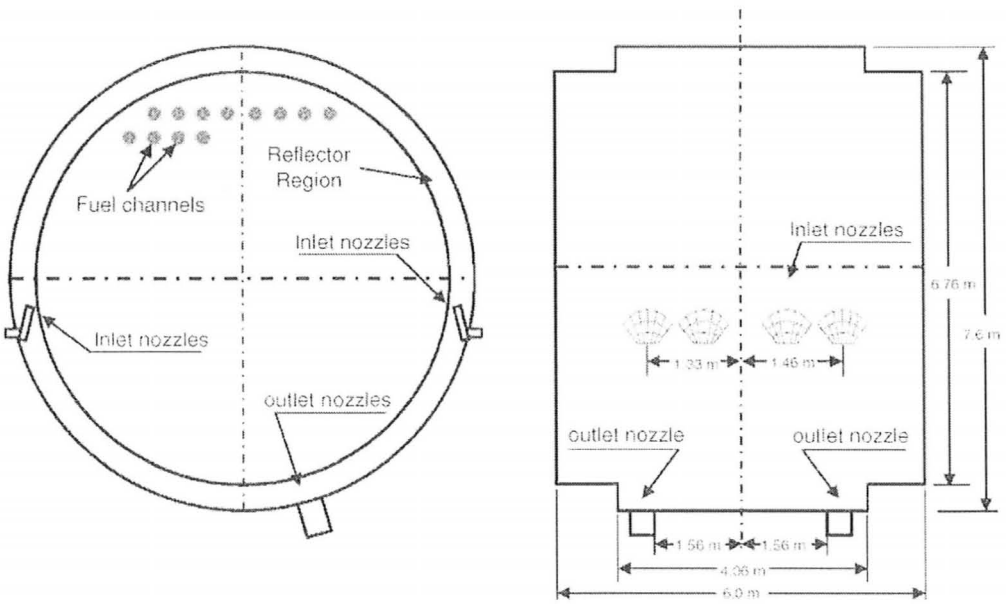

Figure 1.1: Calandria vessel (Kim *et al.*, 2005)

There is a coaxial cylindrical core region inside the calandria shell with a smaller diameter of 6.3 m containing either 380 (CANDU-6) or 480 (Darlington/Bruce) fuel channels displacing about 10% of the total vessel volume. Each fuel channel consists of an outer calandria tube (CT) surrounding a coaxial pressure tube (PT), in which 12 fuel bundles are installed and the heavy water coolant removes heat from the fuel bundles. Four inlet nozzles are located at the middle of the left and right

sidewall, pointing upward. The moderator fluid is discharged through two outlet nozzles at the bottom of the tank and cooled by the moderator heat exchangers before returning through the inlet nozzles. The inlet velocity is about 2 m/s and the outlet velocity is between 5 and 7 m/s (Szymanski *et al.*, 1983). The heat generation rate inside the moderator is up to 900 kW/m^3 in the fuel channel region and about 100 kW/m^3 in the reflector region. Under these conditions the flow field is generally turbulent (Szymanski *et al.*, 1983).

1.2 Aspects of a Critical Break LOCA

The CANDU reactor safety research program in Canada has a strong focus on developing and verifying computer models that predict the reactor process and safety systems accurately during accident situations. Heavy water moderator surrounding each fuel channel is one of the important features in CANDU reactors that acts as a heat sink for the fuel in the situations where other means of heat removal fail. A loss of Coolant Accident (LOCA) caused by a break in one of the primary heat transport system pipes is one of the most safety significant accidents in water reactors and can be the precursor to more serious accidents. During postulated LOCAs, for a particular break size and location referred to as critical break LOCA, the coolant flow through a portion of the reactor core stagnates before the emergency coolant injection restores fuel cooling. In addition, the emergency coolant injection system may fail to operate. In such cases, fuel cooling becomes severely degraded due to rapid flow reduction in the affected flow pass of the heat transport system. This can result in pressure tubes experiencing significant heatup while coolant pressure is still high, thereby causing uniform thermal creep strain (ballooning) of the PT into

contact with its CT (Luxat, 2007). Contact of the hot PT with the CT leads to rapid redistribution of stored heat from the PT to CT and a large spike in heat flux from the CT to the moderator fluid. For lower subcooling conditions of the moderator, dryout of the CT can occur (Figure 1.2).

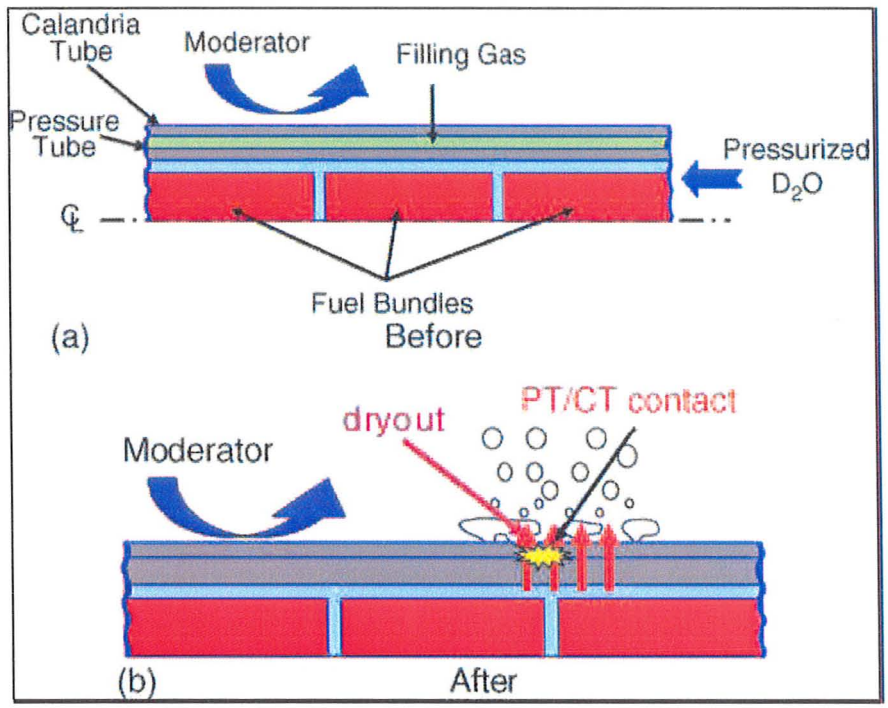

Figure 1.2: PT/CT contact phenomena: (a) before and (b) after (Kim *et al.*, 2005)

The focus of our research is to establish a Computational Fluid Dynamics (CFD) model for predicting the moderator flow field and temperature distribution around one single channel to investigate the potential of dryout occurrence on the CT surface following a PT/CT contact.

1.3 Literature Review

Experimental studies on the flow and temperature distribution inside the moderator have been performed in Canada since the early 1980s. The moderator temperature was measured by Austman *et al.* (1985). They inserted thermo-couples through a shut-off rod guide tube in operating CANDU reactors at Bruce A and Pickering. In the Stern Laboratories in Canada, Huget *et al.* (1989, 1990) performed 2D moderator circulation tests. They observed three distinct flow patterns, corresponding to different ranges of Archimedes number. Khartabil *et al.* (2000) performed 3D moderator circulation tests in the moderator temperature facility (MTF) in the Chalk River Laboratories of Atomic Energy of Canada Limited. These tests had been conducted along with separate effect tests such as a hydraulic resistance through tube bundles, velocity profiles at an inlet diffuser, flow development along a curved wall and the turbulence generation by temperature differences.

Gillespie (1981) described a simple one dimensional model for thermal behavior of a fuel channel when the internal pressure is high enough to deform the PT into contact with its CT. He compared these predictions with his related experimental results in which the pressure tube segment is pressurized and heated at a constant rate into contact with a surrounding calandria tube. The author developed the computer program WALLR. In this program the transient heat conduction equation between the pressure tube and calandria tube is solved in the radial direction by a standard one dimensional, finite element subroutine called WALL. For the boundary conditions he specified a heat flux on the inside surface of the pressure tube. For the pressure tube-calandria tube interface he defined the contact conductance h_c as $h_c = q/(T_{po} - T_{ci})$,

where q is the heat flux, T_{po} is the pressure tube outside surface temperature and T_{ci} is the calandria tube inner surface temperature. The author specified the Heat transfer between the outer surface of the calandria tube and surrounding water by $q = h_b(T_{co} - T_b)$, where T_{co} is the calandria tube outer surface temperature, T_b is the bulk water temperature and h_b depends on type of heat transfer at the outer surface of the calandria tube. Comparing the model predictions with the experimental results, the author concluded that the computer program WALLR predictions for the experiments with an internal pressure of more that $1MPa$ is qualitatively accurate. He found the maximum temperature of the top of the calandria tube when the film boiling covered over most of the surface. He also found out that the film patches cooled and rewet due to heat transfer to regions of nucleate boiling.

Szymanski *et al.* (1983) developed a thermal-hydraulic code, called MODTURC as a modification of the older code MODCIR (Choo, 1980; Austman, 1982), to calculate the moderator temperature and velocity distribution in the calandria of a CANDU reactor. They used the finite difference technique and $k - \varepsilon$ turbulence model to solve three dimensional equations for one quarter of the vessel which was assumed to be symmetric. They also compared the code predictions to experimental results of one reactor design and found a better agreement than previous predictions without turbulence modeling.

Based on these works, a CFD (Computational Fluid Dynamics) code MODTURC-CLAS (Moderator TURbulent Circulation Co-Located Advanced Solution) has been developed by Ontario Power Generation (OPG) and selected as a component of the

Canadian Industry Standard Toolset (IST) for safety analysis. On the other hand, CFD models based on commercial software packages have been developed by others for predicting the CANDU-6 moderator temperature.

Yoon *et al.* (2006) developed a CFD model with a porous media approach for the core region in order to predict the moderator circulation inside the calandria of CANDU reactor under normal operating conditions and LOCA transients, using CFX-4 code (ANSYS Inc.). The authors assumed the moderator to be incompressible and single phase. They modeled the buoyancy forces by the Boussinesq approximation in which the density is considered to be a linear function of the temperature. Using the single channel analysis by the CATHENA and the CHAN-IIA, the authors obtained the transient heat load to the moderator which was implemented as source terms of the energy equation at the location of each channel.

Kim *et al.* (2005) investigated the moderator thermalhydraulic characteristics using the FLUENT code. They modeled all the calandria tubes as heating pipes without any approximation for the core region and investigated the moderator thermalhydraulic characteristics using their optimized model. The authors predicted three flow patterns inside the moderator , i.e., momentum dominated flow, buoyancy dominated flow and mixed type flow depending on the inlet flow rate, heat load, or both. They concluded that since the moderator has enough coolability as the alternate heat sink, the flow pattern does not undergo significant changes, the fuel channel integrity can be assured, and no boiling occurs. The typical flow patterns obtained by Kim *et al.* (2005) are shown in Figure 1.3.

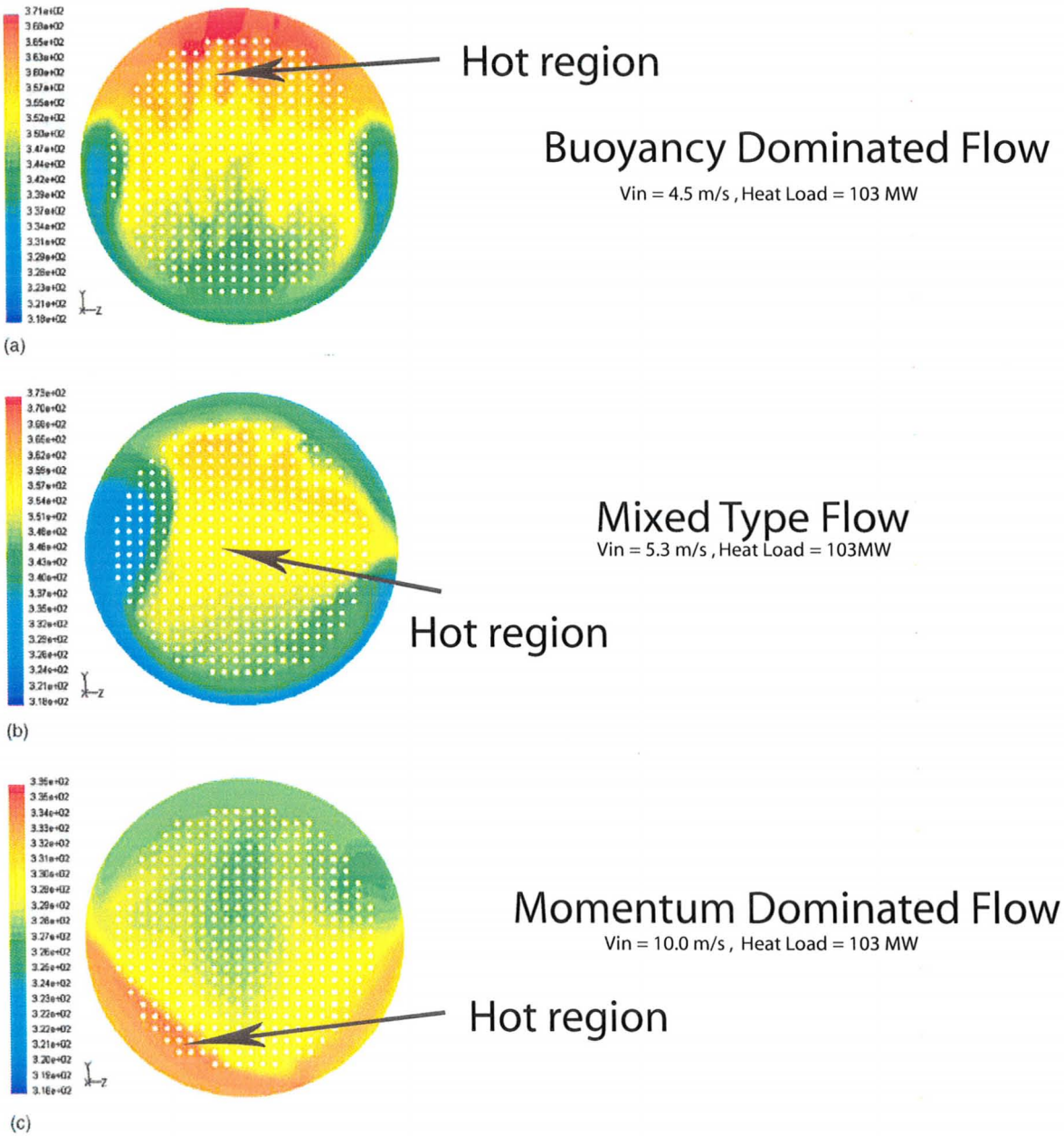

Figure 1.3: Typical flow patterns for CANDU6 moderator (Kim *et al.*, 2005)

The computer programs developed to assess the effect of heat transfer on the CT surface after a postulated PT/CT ballooning contact such as WALLR (Gillespie, 1981) and CATHENA (Fan, 2004) are one-dimensional codes and predict film boiling completely around the circumference of the CT. This does not happen in the experiments. In the experiments the calandria tube surface had patches of film boiling surrounded by patches of nucleate boiling. Therefore in this study the simulation has been performed in two dimension.

In addition, in other studies in 2D or 3D, the whole calandria has been modeled. However, it is a concern that when PT/CT contact occurs in a channel, local moderator boiling may lead to CT dryout and may affect the flow around the CTs at higher elevations. This can detrimentally affect channel integrity if the CT post-dryout temperature becomes sufficiently high to result in thermal creep strain deformation. According to the importance of local prediction of flow and temperature distribution around a single channel, this study has been performed in order to investigate the local thermalhydraulic conditions at the calandria tube wall that will influence potential dryout. This problem has been analyzed using the general purpose finite element code COMSOL.

1.4 Finite Element

The finite element method (FEM) is a numerical technique for finding approximate solutions of partial differential equations (PDE) as well as for integral equations. The solution approach is based on either eliminating the differential equation completely

(steady state problems), or rendering the PDE into an approximating system of ordinary differential equations, which are then numerically integrated using standard techniques such as Euler's method, Runge-Kutta, etc.

In solving partial differential equations, the primary challenge is to create an equation that approximates the equation to be studied, but is numerically stable, meaning that errors in the input data and intermediate calculations do not accumulate and cause the resulting output to be meaningless. In FEM model the geometry is partitioned into small units of a simple shape called mesh elements. Inside the mesh elements each dependent variable can be approximated with a function which can be described with a finite number of parameters, the so called Degree Of Freedom (DOF).

In this study the software package COMSOL (2008), is used for the thermal-hydraulic analysis of the CANDU moderator circulation around one single channel in a transient condition after a postulated PT/CT contact. In such condition, a large amount of heat transfers to the moderator which could lead to sustained CT dryout. Since the accident could occur in different locations inside the moderator and the flow distribution depends on the position of the channel, two kinds of initial flow are considered i.e. upward flow and downward flow. Therefore, the differences in buoyancy effects for upward and downward flow can be taken into account.

Chapter 2

Background

In this chapter a brief description of the modeling and calculations, required to perform a Computational Fluid Dynamics (CFD) simulation are introduced. Some flow characteristics and important definitions in CFD modeling are described. Subsequently, the equations for mass conservation, momentum conservation and energy conservation are introduced. Then the turbulence modeling and two well known turbulent models, $k-\epsilon$ and $k-\omega$ are also explained.

2.1 A Basic Introduction

Heat can be transferred by the mechanisms of conduction, convection and radiation. Conduction arises from transfer of heat through a solid or stationary fluid due to molecular diffusion of energy. Fourier's Law describes conduction heat flux using:

$$q'' = -\mathrm{k}\nabla T \tag{2.1}$$

where q'' is the heat flux $[W/m^2]$, k is the thermal conductivity $[W/m/K]$ and

∇T is the temperature gradient [K/m].

Convection is the heat transfer mechanism from a surface to a fluid that is moving relative to the surface due to advection and diffusion. Fluid and thermal boundary layers are important parts of convection heat transfer. Newton's law of cooling describes convective cooling using:

$$q'' = h(\triangle T) \tag{2.2}$$

where q'' is the heat flux through the surface $[W/m^2]$, h is the convective heat transfer coefficient $[W/m^2/K]$ and $\triangle T$ is the temperature difference between the heat transfer surface and the cooling medium.

Accurate prediction of heat transfer coefficient is the most important issue in convection problems. The heat transfer coefficient depends on surface roughness and geometry as wall as other parameters such as fluid density, velocity, viscosity, thermal conductivity and specific heat capacity which are dependent to the temperature. Furthermore if boiling occurs in the fluid other parameters may affect the heat transfer coefficient. These parameters are the latent heat of vaporization, saturation pressure, vapor fraction, mass quality, liquid to vapor density ratio and surface tension.

In many cases convection can be classified into forced and natural convection modes. In forced convection, the fluid flow is due to external forces. This is the primary mode of heat removal from fuel in nuclear reactors. In natural convection, the flow of fluid is due to buoyancy forces induced by density differences arising from

temperature changes in the fluid.

Radiation is the mechanism for heat transport between surfaces due to electromagnetic waves. Since conduction and convection are predominant in moderator heat transfer, this study excludes radiation.

Dimensionless numbers are widely applied in the field of thermalhydraulics to describe certain phenomena by relating dimensionless combinations of physical variables. The Reynolds number is one of the most important dimensionless numbers:

$$Re = \frac{\mathbf{u}D}{\nu} \tag{2.3}$$

where $\mathbf{u}$ is the velocity, D is the characteristic length and ν is the kinematic viscosity. The Reynolds number gives the ratio of inertial forces to viscous forces and can also be used for determining whether a flow will be laminar or turbulent. Laminar flow occurs at low Reynolds numbers, where viscous forces are dominant, and is characterized by smooth, constant fluid motion. On the other hand, turbulent flow occurs at high Reynolds numbers and is dominated by inertial forces, producing random eddies, vortices and other flow fluctuations. The transition between laminar and turbulent flow is often indicated by a critical Reynolds number (Re_{crit}), which strongly depends on the flow configuration and must be determined experimentally. Within this region there is a gradual transition where the flow is neither fully laminar nor fully turbulent, and predictions of fluid behavior can be difficult.

Prandtl Number is another important dimensionless number approximating the

ratio of thermal diffusivity to momentum diffusivity and is defined as:

$$Pr = \frac{\mu C_p}{\mathrm{k}} \tag{2.4}$$

where k is the thermal conductivity, μ is the viscosity and C_p is the specific heat at constant pressure. The physical importance of Prandtl number for laminar flow is that it represents the relative thickness of the thermal to momentum boundary layer. When Pr is small, it means that the heat diffuses very quickly compared to the velocity (momentum).

The dimensionless heat transfer coefficient, Nusselt number, is equal to the dimensionless temperature gradient at the surface and it measures the convection heat transfer at the surface:

$$Nu = \frac{hD}{\mathrm{k}} \tag{2.5}$$

where h is the convective heat transfer coefficient, D is the characteristic length and k is the thermal conductivity of the fluid.

2.1.1 Viscosity

Viscosity is a quantity that indicates how the fluid responds to the shearing stresses and how easily one layer of the fluid slips over another (see Figure 2.1).

For laminar flow through parallel plates, shown in Figure 2.1, the net external force F parallel to the $x-axis$ produces relative motion between the layers and there

will be a rate change of velocity with distance in the y direction.

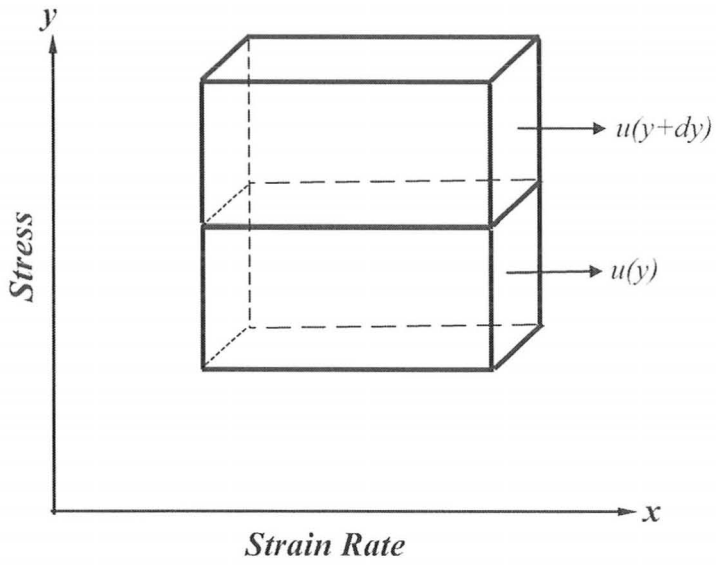

Figure 2.1: Newtonian Concept of Viscosity

It is hypothesized that

$$F \propto A\frac{du}{dy} \tag{2.6}$$

where A is the surface area of the contact between the layers. The proportionality constant is defined as the fluid viscosity and is usually denoted by μ:

$$F = \mu A\frac{du}{dy} \tag{2.7}$$

The shear stress is then equal to force per unit area:

$$\tau = \frac{F}{A} = \mu\frac{du}{dy} \tag{2.8}$$

This is known as Newton's law of viscosity.

Customarily, fluids can be classified as Ideal non-viscous ($\mu = 0$), Newtonian (μ is constant) or non-Newtonian (μ is variable). Although no fluid is ideal, under certain circumstances some fluids approach ideal conditions. Many familiar fluids, such as water and air, are Newtonian fluids while some materials such as emulsions and slurries and some visco-elastic materials, such as blood and some polymers, are classified as non-Newtonian fluids. These materials also include sticky liquids such as latex and honey.

2.1.2 Laminar and Turbulent Flow

One of the important parameters in convection heat transfer problems is to determine whether the boundary layer is laminar or turbulent, since it strongly affects the shear stresses and heat transfer coefficient. Laminar flow occurs at low flow rates where the internal forces due to viscous shear stresses are relatively low. In the laminar boundary layer it is possible to define streamlines along which particles move and fluid motion is characterized by velocity components. By increasing the velocity the shear stress increases and some unsteadiness develops in the perpendicular axis to the flow direction, which is termed the transitional flow region. At higher velocities the velocity components in the perpendicular axis become irregular and turbulent flow region develops. In turbulent boundary layers the fluid motion is characterized by velocity fluctuations which increase the transfer of momentum, energy and consequently surface friction as well as the convection heat transfer rate.

2.1.3 Compressible and Incompressible Flow

All fluids are compressible to some extent, that is the fluid density changes with pressure or temperature, and hence, the more general compressible flow equations must be applied. However, for situations where the changes in pressure and temperature are sufficiently small, the density changes are negligible and the flow can be modeled as an incompressible flow. In the case of constant density:

$$\frac{D\rho}{Dt} = 0 \tag{2.9}$$

where the operator,

$$\frac{D\rho}{Dt} \equiv \frac{\partial\rho}{\partial t} + \mathbf{u}.\nabla\rho \qquad or \qquad \frac{D\rho}{Dt} \equiv \frac{\partial\rho}{\partial t} + u\frac{\partial\rho}{\partial x} + v\frac{\partial\rho}{\partial y} \tag{2.10}$$

where, $\mathbf{u} = u\hat{i} + v\hat{j}$ in a two-dimensional system.

2.1.4 The Convection Boundary Layers

Convention transfer is determined by the boundary layers that develop on the surface. When fluid particles are in direct contact with the surface their velocity is considered as zero. These particles then act to retard the motion of particles in the adjoining fluid layers within the boundary layer thickness δ. This retardation of fluid motion is due to the shear stresses. With increasing distance from the surface, the velocity of the fluid increases until it approaches the free stream value, u_∞. In fact the fluid flow is described by two distinct regions, i.e. the boundary layer in which velocity gradients and shear stresses are large and a region outside the boundary layer in which velocity gradients and shear stresses are negligible. Due to the relation to the fluid

velocity, this boundary layer is called as the velocity boundary layer. If the fluid free stream and surface temperatures differ, a thermal boundary layer also develops over the surface. Fluid particles in contact with the surface achieve thermal equilibrium at the surface temperature and also exchange energy with the adjacent fluid layer and temperature gradients develop in the fluid. This region in which temperature gradients exist in the fluid is the thermal boundary layer. The conditions in the thermal boundary layer strongly affect the wall temperature and determine the heat transfer coefficient.

2.2 Basic Equations in Thermalhydraulics

The governing equations which describe the physics of fluid motion, boundary layer behavior and the convection heat transfer are derived in this section. There are four basic equations which describe the flow; the continuity equation, two components of the momentum equation for 2D problem and the energy equation. In turbulent flow the situation is more complex and is discussed in subsequent sections.

2.2.1 Equation of Continuity

For simplification, a two-dimensional steady flow is assumed for which x is the direction along to the surface and y is normal to the surface. The control volume is of unit depth in the z direction.

Applying the principle of conservation of mass, we get:

$$\frac{\partial}{\partial t}\int_V \rho dV = \int_S -\rho \mathbf{u}.\hat{\mathbf{n}} dS \tag{2.11}$$

where $\hat{\mathbf{n}}$ is the outward unit normal to the surface. Using Gauss' Divergence theorem which is:

$$\int_S \mathbf{F}.\hat{\mathbf{n}} dS = \int_V \nabla.\mathbf{F} dV \tag{2.12}$$

Equation (2.11) becomes:

$$\int_V \frac{\partial \rho}{\partial t} dV = \int_V -\nabla.(\rho \mathbf{u}) dV \qquad \Rightarrow \qquad \int_V [\frac{\partial \rho}{\partial t} + \nabla.(\rho \mathbf{u})] dV = 0 \tag{2.13}$$

therefore we get:

$$\frac{\partial \rho}{\partial t} + \nabla.(\rho \mathbf{u}) = 0 \qquad \Rightarrow \qquad \frac{\partial \rho}{\partial t} + \mathbf{u}.\nabla \rho + \rho \nabla.\mathbf{u} = 0 \tag{2.14}$$

and finally we get the conservation of mass equation or the continuity equation which is:

$$\frac{D\rho}{Dt} + \rho \nabla.\mathbf{u} = 0 \tag{2.15}$$

In the case of incompressible flow, by applying Equation (2.9), the continuity equation becomes:

$$\nabla.\mathbf{u} = 0 \qquad or \qquad \frac{\partial u}{\partial x} + \frac{\partial v}{\partial y} = 0 \tag{2.16}$$

2.2.2 Equations of Motion

Motion of the fluid particles is influenced by the forces acting on it which can be divided into two groups, i.e. external and internal forces. External forces such as gravitational and body forces are from outside of the fluid acting on a local portion of it while internal forces are due to the interaction between neighboring fluid particles. External forces are expressed as a force per unit mass, $\mathbf{F}$ and in a control volume of the fluid, δV, mass is $\rho\delta V$ with associated external or body force of $\mathbf{F}\rho\delta V$. We designate the x and y component of this force per unit volume of fluid as F_x and F_y, respectively. Internal forces, $\mathbf{F}_s$ are expressed as forces per unit area or stresses and are applied across the boundary surface between elements. Theses forces are due to the fluid static pressure as well as to viscous stresses which consist of two perpendicular components including a normal stress, σ_{ii}, and a shear stress, τ_{ij}. (Figure 2.2)

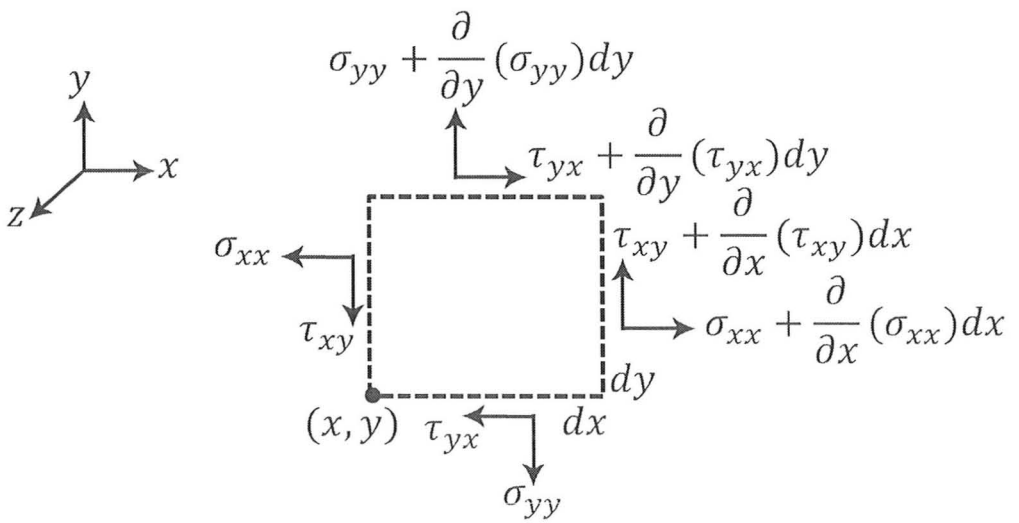

Figure 2.2: Normal and shear viscous stresses for a control volume ($dx.dy$) in 2D

Considering Figure 2.2 in the x direction, the normal stress σ_{xx} corresponds to a force component normal to the surface while the shear stress τ_{xy} corresponds to a shear force along the surface in y direction. According to the Figure 2.2 all of the stress components are positive due to the fact that both the surface normal and the force component are in the same direction. Therefore the normal viscous stresses are tensile stresses while the static pressure produced by external forces which acts on the fluid in the control volume is a compressive stress. The net internal force in each direction using a Taylor series expansion can be derived as (Incropera, 1990):

$$F_{s,x} = (\frac{\partial \sigma_{xx}}{\partial x} - \frac{\partial p}{\partial x} + \frac{\partial \tau_{yx}}{\partial y})dxdy \tag{2.17}$$

$$F_{s,y} = (\frac{\frac{\partial \tau_{xy}}{\partial x} + \partial \sigma_{yy}}{\partial y} - \frac{\partial p}{\partial y})dxdy \tag{2.18}$$

Newton's second law of motion is applied for the control volume which states that the sum of all forces acting on the control volume is equal the net rate at which momentum leaves the control volume.

The fluid momentum fluxes on the x direction due to mass flow through both x and y surfaces are shown in Figure 2.3 which may change in each of the coordinate directions. The net rate at which x momentum leaves the control volume is:

$$\frac{\partial[(\rho u)u]}{\partial x}dx(dy) + \frac{\partial[(\rho v)u]}{\partial y}dy(dx) \tag{2.19}$$

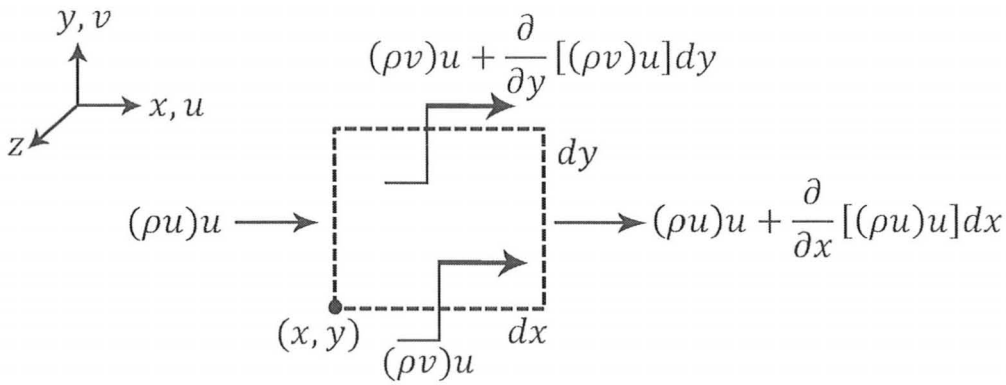

Figure 2.3: Momentum fluxes for a control volume ($dx.dy$) in 2D

Now by equating the sum of the forces in the x direction to the rate of change in the x momentum and using the continuity Equation (2.15), we get the equation of motion in the x direction:

$$\rho(u\frac{\partial u}{\partial x} + v\frac{\partial u}{\partial y}) = \frac{\partial}{\partial x}(\sigma_{xx} - p) + \frac{\partial \tau_{yx}}{\partial y} + F_x \tag{2.20}$$

In a similar way the equation of motion is obtained for the y direction:

$$\rho(u\frac{\partial v}{\partial x} + v\frac{\partial v}{\partial y}) = \frac{\partial \tau_{xy}}{\partial x} + \frac{\partial}{\partial y}(\sigma_{yy} - p) + F_y \tag{2.21}$$

In the Equations (2.20) and (2.21), the left hand side represents the net rate of momentum flow from the control volume and the right hand side consists of the net external forces (body force) and internal forces (viscous and pressure forces). For a Newtonian fluid, the linear relation between stresses and velocity gradients is (Burmeister, 1993):

$$\sigma_{xx} = 2\mu\frac{\partial u}{\partial x} - \frac{2}{3}\mu\nabla.\mathbf{u} \tag{2.22}$$

$$\sigma_{yy} = 2\mu\frac{\partial v}{\partial y} - \frac{2}{3}\mu\nabla.\mathbf{u} \tag{2.23}$$

$$\tau_{xy} = \tau_{yx} = \mu(\frac{\partial u}{\partial y} + \frac{\partial v}{\partial x}) \tag{2.24}$$

Introducing Equations (2.22), (2.23) and (2.24) into the Equations of motion (2.20) and (2.21) which follow the Newton's second law gets:

$$\rho(u\frac{\partial u}{\partial x} + v\frac{\partial u}{\partial y}) = -\frac{\partial p}{\partial x} + \frac{\partial}{\partial x}\{\mu[2\frac{\partial u}{\partial x} - \frac{2}{3}\nabla.\mathbf{u}]\} + \frac{\partial}{\partial y}[\mu(\frac{\partial u}{\partial y} + \frac{\partial v}{\partial x})] + F_x \tag{2.25}$$

$$\rho(u\frac{\partial v}{\partial x} + v\frac{\partial v}{\partial y}) = -\frac{\partial p}{\partial y} + \frac{\partial}{\partial y}\{\mu[2\frac{\partial v}{\partial y} - \frac{2}{3}\nabla.\mathbf{u}]\} + \frac{\partial}{\partial x}[\mu(\frac{\partial u}{\partial y} + \frac{\partial v}{\partial x})] + F_y \tag{2.26}$$

Assuming a constant viscosity, the x-direction equation of motion is:

$$\begin{aligned}\rho(u\frac{\partial u}{\partial x} + v\frac{\partial u}{\partial y}) = -\frac{\partial p}{\partial x} + \mu\{[\frac{\partial(\partial u/\partial x)}{\partial x} + \frac{\partial(\partial u/\partial y)}{\partial y}]+ \\ [\frac{\partial(\partial u/\partial x)}{\partial x} + \frac{\partial(\partial v/\partial x)}{\partial y}] - \frac{2}{3}\frac{\partial\nabla.\mathbf{u}}{\partial x}\} + F_x\end{aligned} \tag{2.27}$$

The second bracketed term inside the braces is $\nabla.\mathbf{u}$ if the order of differentiation is interchanged for each term. Then the x-direction equation of motion becomes:

$$\rho(u\frac{\partial u}{\partial x}+v\frac{\partial u}{\partial y})=-\frac{\partial p}{\partial x}+\mu[\frac{\partial^2 u}{\partial x^2}+\frac{\partial^2 u}{\partial y^2}+\frac{1}{3}\frac{\partial \nabla.\mathbf{u}}{\partial x}] \tag{2.28}$$

According to the above equations we can obtain the general form of the equation of motion for the constant viscosity case as:

$$\rho\frac{D\mathbf{u}}{Dt}=\mathbf{F}-\nabla p+\mu[\nabla^2\mathbf{u}+\frac{1}{3}\nabla(\nabla.\mathbf{u})] \tag{2.29}$$

In the case of incompressible flow applying the Equation (2.16) we get the equations of motion as:

$$\rho\frac{Du}{Dt}=F_x-\frac{\partial p}{\partial x}+\mu(\frac{\partial^2 u}{\partial x^2}+\frac{\partial^2 u}{\partial y^2}) \tag{2.30}$$

$$\rho\frac{Dv}{Dt}=F_y-\frac{\partial p}{\partial y}+\mu(\frac{\partial^2 v}{\partial x^2}+\frac{\partial^2 v}{\partial y^2}) \tag{2.31}$$

In vector notation the above set of Equations (2.30) and (2.31) describing the motion of a constant density and viscosity fluid are written as:

$$\rho\frac{D\mathbf{u}}{Dt}=\mathbf{F}-\nabla p+\mu\nabla^2\mathbf{u} \tag{2.32}$$

This is known as the Navier-Stokes equation.

2.2.3 Energy Equation

A general form of energy conservation on a rate basis can be expressed as below:

$$\dot{E}_{in}+\dot{E}_g-\dot{E}_{out}=\frac{dE_{st}}{dt}\equiv\dot{E}_{st} \tag{2.33}$$

where $\dot{E}_{in}$ and $\dot{E}_{out}$ are the rate at which thermal and mechanical energy enter and leave the control volume respectively through the control surface. $\dot{E}_g$ is the rate at which thermal energy may be generated due to conversion from other energy forms. $\dot{E}_{st}$ or $\frac{dE_{st}}{dt}$ expresses the rate of change of energy stored within the control volume. By integrating Equation (2.33) over time we obtain the following energy conservation equation for a time interval $\triangle t$:

$$E_{in} + E_g - E_{out} = \triangle E_{st} \tag{2.34}$$

Neglecting potential energy effects, the energy per unit mass of the fluid includes the internal energy, e, and the kinetic energy, $\frac{1}{2}V^2$, where $V^2 = u^2 + v^2$. For the control volume shown in Figure 2.4 we have an advection energy transfer with the bulk fluid motion as well as a conduction energy transfer across the control surfaces.

The net rate transfer of energy into the control volume in the x direction for each case is:

$$\begin{aligned} \dot{E}_{adv,x} - \dot{E}_{adv,x+dx} \equiv \rho u(e + \frac{V^2}{2})dy - \{\rho u(e + \frac{V^2}{2}) \\ + \frac{\partial}{\partial x}[\rho u(e + \frac{V^2}{2})]dx\}dy = -\frac{\partial}{\partial x}[\rho u(e + \frac{V^2}{2})]dxdy \end{aligned} \tag{2.35}$$

$$\dot{E}_{cond,x} - \dot{E}_{cond,x+dx} = -(k\frac{\partial T}{\partial x})dy - [-k\frac{\partial T}{\partial x} - \frac{\partial}{\partial x}(k\frac{\partial T}{\partial x})dx]dy = \frac{\partial}{\partial x}(k\frac{\partial T}{\partial x})dxdy \tag{2.36}$$

Work interactions involving the internal and external forces may also transfer energy to and from the fluid in the control volume and its net rate in the x direction

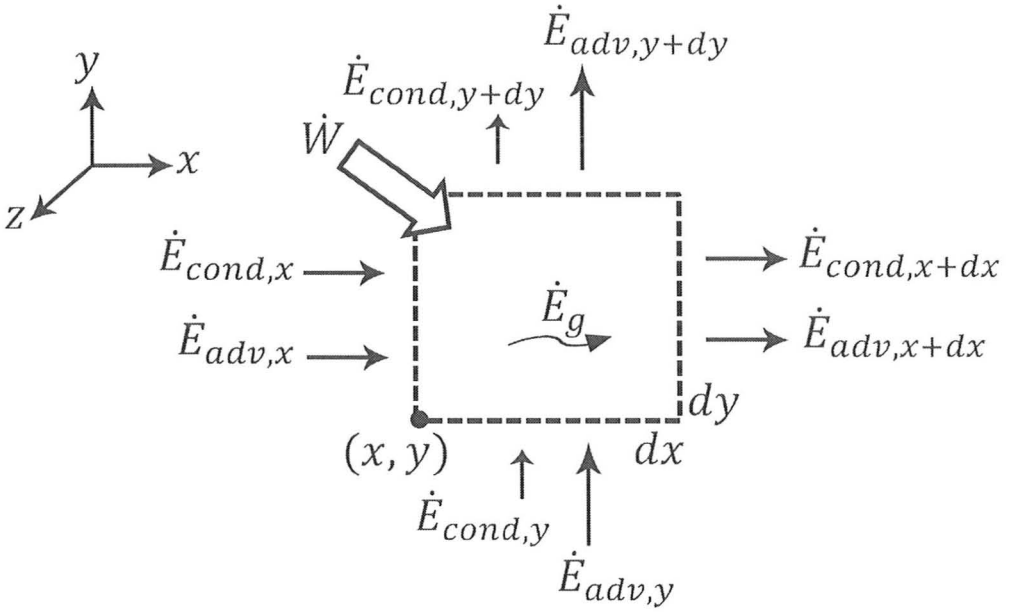

Figure 2.4: Energy conservation for a control volume ($dx.dy$) in 2D

can be expressed as:

$$\dot{W}_{net,x} = (F_x u)dxdy + \frac{\partial}{\partial x}[(\sigma_{xx} - p)u]dxdy + \frac{\partial}{\partial y}(\tau_{yx} u)dxdy \tag{2.37}$$

where the first term in the right hand side is the work done by external forces (body forces) and the two other terms account for the net work done by the pressure and viscous forces.

Applying Equations (2.36), (2.35) and (2.37) with analogous equations for the y direction, the Equation (2.33) becomes:

$$\begin{aligned} -\frac{\partial}{\partial x}[\rho u(e+\frac{V^2}{2}] - \frac{\partial}{\partial y}[\rho v(e+\frac{V^2}{2}] + \frac{\partial}{\partial x}(k\frac{\partial T}{\partial x}) + \frac{\partial}{\partial y}(k\frac{\partial T}{\partial y}) + (F_x u + F_y v) \\ -\frac{\partial}{\partial x}(\rho u) - \frac{\partial}{\partial y}(\rho v) + \frac{\partial}{\partial x}(\sigma_{xx}u + \tau_{xy}v) + \frac{\partial}{\partial y}(\tau_{yx}u + \sigma_{yy}v) + \dot{q} = 0 \end{aligned} \tag{2.38}$$

where $\dot{q}$ is the energy generated rate per unit volume. Equation (2.38) represents mechanical and thermal energy in the control volume. In order to solve heat transfer problems it is more convenient to obtain the thermal energy equation by multiplying Equation (2.20) and (2.21) by u and v, respectively, and subtracting the result from Equation (2.38) which after considerable manipulation gives the following equation:

$$\rho u\frac{\partial e}{\partial x} + \rho v\frac{\partial e}{\partial y} = \frac{\partial}{\partial x}(k\frac{\partial T}{\partial x}) + \frac{\partial}{\partial y}(k\frac{\partial T}{\partial y}) - p(\frac{\partial u}{\partial x} + \frac{\partial v}{\partial y}) + \mu\Phi + \dot{q} \tag{2.39}$$

where $\mu\Phi$ is the viscous dissipation which accounts for the rate at which mechanical energy is irreversibly converted to thermal energy due to viscous effects in the fluid and is defined as:

$$\mu\Phi \equiv \mu\{(\frac{\partial u}{\partial y} + \frac{\partial v}{\partial x})^2 + 2[(\frac{\partial u}{\partial x})^2 + \frac{\partial v}{\partial y})^2] - \frac{2}{3}(\frac{\partial u}{\partial x} + \frac{\partial v}{\partial y})^2\} \tag{2.40}$$

According to the above equations the general form of the energy equation in vector notation can be expressed as:

$$\rho\frac{De}{Dt} = \nabla.(k\nabla T) - p(\nabla.\mathbf{u}) + \mu\Phi + \dot{q} \tag{2.41}$$

The enthalpy, H, per unit mass is introduced as a replacement for thermal internal

energy, e, for a more convenient form of the energy equation. By definition:

$$H = e + \frac{p}{\rho} \tag{2.42}$$

therefore

$$\frac{De}{Dt} = \frac{DH}{Dt} - \frac{1}{\rho}\frac{Dp}{Dt} + \frac{p}{\rho^2}\frac{D\rho}{Dt} \tag{2.43}$$

Referring to the continuity Equation (2.15), the last term in the right hand side of the above relation equals $-p\rho^{-1}\nabla.\mathbf{u}$. Incorporating of this fact into Equation (2.43) and substituting the result into Equation (2.41) one obtains:

$$\rho\frac{DH}{Dt} = \nabla.(k\nabla T) + \frac{Dp}{Dt} + \mu\Phi + \dot{q} \tag{2.44}$$

Due to the fact that it is more common for a fluid to undergo a nearly constant pressure process (for which $\frac{Dp}{Dt} = 0$), the term $\frac{Dp}{Dt}$ in Equation (2.44) is often preferred over the term $p(\nabla.\mathbf{u})$ in Equation (2.41).

Referring to thermodynamics and recalling the definition of the specific heat capacity at constant pressure, C_p , and the thermal expansion coefficient, β, (Burmeister, 1993):

$$C_p = \frac{\partial H}{\partial T}\,|_{p=const} \tag{2.45}$$

$$\beta = -\frac{1}{\rho}(\frac{\partial \rho}{\partial T})_{p=const} \tag{2.46}$$

the energy equation becomes:

$$\rho C_p \frac{DT}{Dt} = \nabla.(k\nabla T) + \beta T \frac{Dp}{Dt} + \mu\Phi + \dot{q} \tag{2.47}$$

For a constant density fluid , $\beta = 0$, and by neglecting the viscous dissipation, $\Phi = 0$, the energy equation becomes:

$$\rho C_p \frac{DT}{Dt} = \nabla.(k\nabla T) + \dot{q} \tag{2.48}$$

2.2.4 Initial and Boundary Conditions

In order to solve the above equations, initial and boundary conditions need to be determined. Initial conditions give the fluid conditions at time $t = 0$ while boundary conditions prescribe the fluid conditions at inlet or outlet boundaries and the surfaces with which the fluid may be in contact. Different boundary conditions may cause quite different results and it should be noted that improper sets of boundary conditions may introduce nonphysical influences on the simulation system. Hence, arranging the boundary conditions for different problems is very important.

2.3 Turbulence Modeling

Numerical modeling can be used in order to predict the behavior of turbulent systems by accounting for the nature of the fluctuations around the mean flow. When flow becomes turbulent, all quantities fluctuate in time and space and an averaged representation almost provides sufficient information about the flow instead of having an exact and detailed picture of the flow. Therefore, due to the random fluctuations

of the various flow properties, in turbulence modeling a statistical approach introduced by Reynolds (1895) is used. In this approach all quantities are expressed as the sum of mean and fluctuating parts and then the time averaged continuity and Navier-Stokes equations are generated. As we will see in this section, the nonlinearity of the Navier-Stokes equation introduces unknown momentum fluxes that act as apparent stresses throughout the flow. Deriving equations for these stresses results in additional unknown quantities. This illustrates the issue of closure problem and establishing of sufficient number of equations for the unknowns.

2.3.1 Reynolds Averaging

Generally, Reynolds averaging is expressed in different forms involving either an integral or a summation. In turbulence modeling the *time average*, the *spatial average* and the *ensemble average* are the most common forms.

Time averaging is appropriate for stationary turbulent flow which, on the average, does not vary with time. For an instantaneous flow variable, f, the time average, $\overline{F_t}$, is defined as:

$$\overline{F_t} = \lim_{\triangle t \longrightarrow \infty} \frac{1}{\triangle t} \int_t^{t+\triangle t} f dt \tag{2.49}$$

Spatial averaging is appropriate for homogeneous turbulent flow, which on the average, is uniform in all directions. By doing a volume integral we average over all spatial coordinates:

$$\overline{F_v} = \lim_{V \longrightarrow \infty} \frac{1}{V} \int\int\int f dV \tag{2.50}$$

Ensemble averaging is the most general type of averaging and for N identical measurements is defined as:

$$\overline{F_E} = \lim_{N \longrightarrow \infty} \frac{1}{N} \sum_{n=1}^{N} f_n \tag{2.51}$$

Due to the inhomogeneous turbulence in the engineering problems, the time averaging is the most common form of Reynolds averaging. The Reynolds-averaged representation of turbulent flow decompose the instantaneous velocity, $\mathbf{u}$, into a mean, $\overline{\mathbf{u}}$ and a fluctuating, $\mathbf{u}'$ component:

$$\mathbf{u} = \overline{\mathbf{u}} + \mathbf{u}' \tag{2.52}$$

According to the Equation (2.49), the quantity $\overline{\mathbf{u}}$ is the time averaged or mean velocity defined by:

$$\overline{\mathbf{u}} = \lim_{\triangle t \longrightarrow \infty} \frac{1}{\triangle t} \int_{t}^{t+\triangle t} \mathbf{u} dt \tag{2.53}$$

The time average of the mean velocity is again the same value:

$$\overline{\overline{\mathbf{u}}} = \lim_{\triangle t \longrightarrow \infty} \frac{1}{\triangle t} \int_{t}^{t+\triangle t} \overline{\mathbf{u}} dt = \overline{\mathbf{u}} \tag{2.54}$$

The time average of the fluctuating component of the velocity is zero:

$$\overline{\mathbf{u}'} = \lim_{\triangle t \longrightarrow \infty} \frac{1}{\triangle t} \int_{t}^{t+\triangle t} [\mathbf{u} - \overline{\mathbf{u}}] dt = \overline{\mathbf{u}} - \overline{\mathbf{u}} = 0 \tag{2.55}$$

However, $\overline{\mathbf{u}'\mathbf{u}'}$ is not necessarily of zero value.

Because the infinite time interval $\triangle t$ is not truly realized in any physical problem, in forming our time average we select a very long time $\triangle t$ relative to the maximum period of the velocity fluctuations, $\triangle t_1$. In addition some flows are not turbulent in nature due to the very slow variations in the mean flow referred to the $\triangle t_2$ as the characteristic time scale. Therefore, the Equations (2.56) and (2.59) must be modified as follows:

$$\mathbf{u} = \overline{\mathbf{u}} + \mathbf{u}' \tag{2.56}$$

In terms of component for a 2-dimensional problem we have:

$$u = \overline{u} + u' \tag{2.57}$$

$$v = \overline{v} + v' \tag{2.58}$$

and

$$\overline{u} = \frac{1}{\triangle t} \int_t^{t+\triangle t} u dt, \qquad \triangle t_1 \ll \triangle t \ll \triangle t_2 \tag{2.59}$$

These concepts are indicated in the Figure 2.5.

If $\overline{\mathbf{u}'\mathbf{u}'} = \overline{\mathbf{v}'\mathbf{v}'}$, the turbulence is isotropic and there is no gradient in the mean velocity $\overline{\mathbf{u}}$. The turbulence is anisotropic when the mean velocity has a gradient.

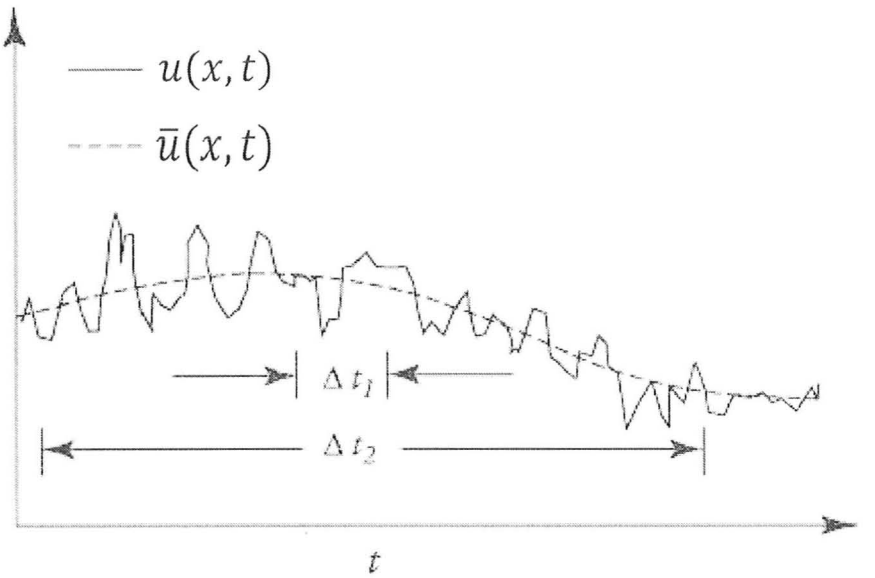

Figure 2.5: Time averaging for nonstationary turbulence

2.3.2 Reynolds-Averaged Navier-Stokes (RANS)

In what follows it is assumed that properties are constant for simplicity. Decomposition of flow fields into a mean and a fluctuating part followed by insertion into the continuity and Navier-Stokes equations and then time averaging, gives the Reynolds-averaged Navier-Stokes (RANS) equations. The continuity Equation (2.16) for the unsteady state case becomes:

$$\frac{\partial(\overline{u}+u')}{\partial x}+\frac{\partial(\overline{v}+v')}{\partial y}=0 \tag{2.60}$$

Time averaging of this equation gives:

$$\overline{\frac{\partial(\overline{u}+u')}{\partial x}+\frac{\partial(\overline{v}+v')}{\partial y}}=0 \tag{2.61}$$

Interchanging the order of operation in space and time gives:

$$\frac{\partial(\overline{\overline{u}} + \overline{u'})}{\partial x} + \frac{\partial(\overline{\overline{v}} + \overline{v'})}{\partial y} = 0 \tag{2.62}$$

Since the time average of the fluctuation term is zero, the time averaged continuity equation becomes:

$$\frac{\partial \overline{u}}{\partial x} + \frac{\partial \overline{v}}{\partial y} = 0 \tag{2.63}$$

or

$$\nabla . \overline{\mathbf{u}} = 0 \tag{2.64}$$

Replacing the instantaneous velocity by the mean velocity, the time-averaged conservation of mass Equation (2.64), is identical to the instantaneous Equation (2.16).

Referring to the Equation (2.20) the unsteady x-momentum in conservation form is:

$$\rho[\frac{\partial u}{\partial t} + \frac{\partial uu}{\partial x} + \frac{\partial vu}{\partial y}] - \rho[\frac{\partial u}{\partial x} + \frac{\partial v}{\partial y}]u = F_x - \frac{\partial p}{\partial x} + \frac{\partial \sigma_{xx}}{\partial x} + \frac{\partial \tau_{yx}}{\partial y} \tag{2.65}$$

Time averaging and interchanging the order of operation in space and time gives:

$$\begin{aligned} \rho[\frac{\partial \overline{u}}{\partial t} + \frac{\partial \overline{u}'}{\partial t} + \frac{\partial(\overline{u}\ \overline{u} + 2\overline{u}\ \overline{u}' + \overline{u'u'})}{\partial x} + \frac{\partial(\overline{v}\ \overline{u} + \overline{v}\ \overline{u}' + \overline{u}\ \overline{v}' + \overline{v'u'})}{\partial y}] \\ = \overline{F}_x + \overline{F}'_x - \frac{\partial(\overline{P} + \overline{P}')}{\partial x} + \frac{\partial(\overline{\sigma}_{xx} + \overline{\sigma}'_{xx})}{\partial x} + \frac{\partial(\overline{\tau}_{yx} + \overline{\tau}'_{yx})}{\partial y} \end{aligned} \tag{2.66}$$

$$\rho(\frac{\partial \overline{u}}{\partial t} + \frac{\partial \overline{u}\ \overline{u}}{\partial x} + \frac{\partial \overline{v}\ \overline{u}}{\partial y}) = \overline{F}_x - \frac{\partial \overline{P}}{\partial x} + \frac{\partial}{\partial x}(\overline{\sigma}_{xx} - \rho\overline{u'u'}) + \frac{\partial}{\partial y}(\overline{\tau}_{yx} - \rho\overline{v'u'}) \quad (2.67)$$

Implementing the continuity equation that $\nabla.\overline{\mathbf{u}} = 0$ then gives:

$$\rho(\frac{\partial \overline{u}}{\partial t} + \overline{u}\frac{\partial \overline{u}}{\partial x} + \overline{v}\frac{\partial \overline{u}}{\partial y}) = \overline{F}_x - \frac{\partial \overline{P}}{\partial x} + \frac{\partial}{\partial x}(\overline{\sigma}_{xx} - \rho\overline{u'u'}) + \frac{\partial}{\partial y}(\overline{\tau}_{yx} - \rho\overline{v'u'}) \quad (2.68)$$

The y momentum equation has the same form as the Equation (2.68). Equation (2.68) is usually referred as the Reynolds Averaged Navier-Stokes (RANS) equation. A comparison with the instantaneous x momentum Equation (2.20), shows that the only difference is the appearance of the Reynolds stress terms in the equation (2.68) which represents the interaction between the fluctuating velocities.

In fact, in Equation (2.68) the total stress is the sum of a molecular $\overline{\tau}_{xy}$ or $\overline{\sigma}_{xx}$ and a turbulent part $-\rho\overline{u'u'}$ or $-\rho\overline{v'u'}$ known as Reynolds stress. We denote the Reynolds stress with τ_{ij}. Thus

$$\tau_{ij} = -\overline{\rho u_i' u_j'} \quad (2.69)$$

This is a symmetric tensor and $\tau_{ij} = \tau_{ji}$ and thus for a 2-dimensional problem it has three independent components. Therefore, after time averaging we have produced three unknown quantities and along with three unknown mean flow properties, i.e. pressure and the two velocity components we have six unknowns. Our equations are mass conservation Equation (2.64) and the two components of Equation (2.68) for

a total of three. This means the system is not closed yet. Therefore in order to obtain the mean flow characteristics, the information about the small-scale structure of the flow needs to be determined. This information is the correlation between the fluctuations in different directions. In order to solve the additional unknowns it is required to impose assumptions about the flow, the so-called closure of the turbulence model.

2.3.3 Boussinesq Eddy Viscosity

By using the Boussinesq eddy viscosity assumption, the momentum transfer caused by turbulent eddies can be modeled with an eddy viscosity. This is an analogy with which the momentum transfer caused by the molecular motion in the fluid can be described by a molecular viscosity. The Boussinesq assumption relates the turbulent Reynolds stress;

$$\tau_{ij} = -\rho\overline{u_i' u'}_j \tag{2.70}$$

to the mean strain;

$$S_{ij} = \frac{1}{2}(\nabla \mathbf{u} + (\nabla \mathbf{u})^T) - \frac{1}{3}\overline{u_k' u'}_k \delta_{ij} \tag{2.71}$$

as a direct proportionality:

$$\tau_{ij} = \mu_T(2S_{ij}) - \frac{1}{3}\overline{u_k' u'}_k \delta_{ij} \tag{2.72}$$

$$\tau_{ij} = 2\mu_T S_{ij} - \frac{2}{3}\rho k \delta_{ij} \tag{2.73}$$

where δ_{ij} is the Kronecker delta, $\mathbf{u}$ is the mean velocity and μ_T is the turbulent eddy viscosity and k is the turbulent kinetic energy. This is assuming the stresses, τ_{ij} are aligned with the strains, S_{ij}. (Pope, 2000)

Turbulence modeling is one of the key parameters in Computational Fluid Dynamics and several models have been developed to model the physical behavior of turbulent flows which is an extremely complicated phenomenon. These models consists of zero-equation models, one-equation models, two-equation models and second order closure models. The two-equation models are the basis in most industrial simulations and computer codes and in this thesis we focus on the most important ones which are $k-\epsilon$ and $k-\omega$ models.

2.3.4 The $k-\epsilon$ Turbulence Model

One of the most studied two-equation turbulence models is the $k-\epsilon$ model in which the turbulent eddy viscosity is obtained by solving partial differential transport equations for the turbulence kinetic energy, k, and the dissipation rate of turbulence energy, ϵ. These transport equations are relatively easy to implement into the existing CFD codes. This model is based on the assumption that the turbulent eddy viscosity is identical for all Reynolds stresses. This assumption is adequate for the calculation of thin shear layers in two-dimensional flows without swirl. However, in some flow problems with strong anisotropy (e.g., preferential strains, rotation, separation, impingement) the isotropic eddy viscosity assumption underpredicts the velocity fluctuations and thus gives inaccurate predictions for the Reynolds stresses. Another limitation of the $k-\epsilon$ turbulence model is the restriction to high Reynolds number

flows (i.e. $Re > 20000$) which makes this model unapplicable to the boundary layers near the walls and to low Reynolds number flows. In many cases, efficient treatment of the near wall region can be done using the common approach of wall functions. However, the standard $k-\epsilon$ model and wall function approach are insufficient for the low Reynolds number flows. The most popular approach for this condition has been developed by Jones and Launder (1972) to provide turbulent equations valid throughout the laminar, semi-laminar and fully turbulent regions. This model requires many additional computations in the near wall region, increased equation complexity and related numerical instability. However, the $k-\epsilon$ turbulence model with an appropriate wall function is the most common approach which is widely applied to practical turbulent flow problems.

In this model, turbulent viscosity is modeled by:

$$\mu_T = \rho C_\mu \frac{k^2}{\epsilon} \tag{2.74}$$

where C_μ is a model constant.

The transport equations of k and ϵ can be derived by taking the trace of the equations for the Reynolds stresses. These equations and the wall functions treatment which is used in this study are determined in Chapter 3.

2.3.5 The $k-\omega$ Turbulence Model

$k-\omega$ turbulence model is the second most widely used two-equation model. Much of the $k-\epsilon$ model's inaccuracy can be attributed to the rather inaccurate modeling

of the turbulence energy dissipation term, ϵ. Hence, in the $k-\omega$ model transport of the dissipation per unit turbulent kinetic energy, ω is modeled as an alternative. Therefore we have:

$$\omega = \frac{\epsilon}{k} \tag{2.75}$$

The turbulent viscosity is modeled by:

$$\mu_T = \rho\frac{k}{\omega} \tag{2.76}$$

The transport equations of k and ω are determined in Chapter 3.

This model works well at the walls without special treatments. In fact this model underpredicts the k peak near the wall but also has $\epsilon = k\omega \rightarrow 0$ at wall (underestimating ϵ)and the net effect is μ_T fairly well estimated. The problem with this model occurs away from the wall where μ_T is overly sensitive to ω in the free stream. Menter (1994) overcame this issue by using a two-zone model: $k-\omega$ near the wall and $k-\epsilon$ away from the wall which is used in CFX.

For a certain flow problem there is no guarantee that one turbulence model provides better results than the other. Generally, the $k-\omega$ model behaves better close to the walls and usually predicts free shear flows more accurately than the $k-\epsilon$ model. Moreover when the curvature is important (around the cylinder) $k-\omega$ is a better model than $k-\epsilon$. On the other hand, for external flows, $k-\omega$ predictions are strongly dependent on the free stream values of k and ω.

Chapter 3

Methodology and Model Description

In this chapter the methodology and the modeling issues with COMSOL are described. COMSOL is an interactive commercial software for modeling scientific and engineering problems based on partial differential equations (PDEs) and solving coupled physics phenomena simultaneously using finite element method (FEM) (COMSOL, 2008). In this study COMSOL code is used in order to solve the governing equations of fluid dynamics in the domain. In this chapter the assumptions and the geometry used in the model are described. Then the governing equations and material properties introduced to the model are illustrated. Later on the specified boundary conditions and mesh are introduced.

3.1 Assumptions

In this model, a single phase fluid inside the moderator and a uniform PT/CT contact has been considered. During normal operation, heat can be deposited to the moderator in two different ways. The first one is by direct heating of neutrons, decay heat from fission products and gamma rays. The second way, which accounts for a small portion of the total heat load, is by heat convection from the surface of fuel channels. The total heat load to the moderator is taken to be 103 MW (about 103%) of full power) consisting of 98.7 MW by volumetric direct heating and 4.3 MW by convective heat from fuel channel surface (Kim *et al.*, 2005). The convective heat transfer to the moderator is assumed to be uniformly with axial direction.

3.2 Model Geometry

The geometry is depicted in Figure 3.1-a. The arrow indicates the flow direction for upward flow. Neglecting any end effects from the walls of the vessel, the solution is constant in the direction of the tubes and therefore the model is reduced to a 2D domain.

The dashed line marks the model region in 2D which is shown in Figure 3.1-b. L denotes the arc-length associated with the angle θ on the surface of the central CT in which PT/CT contact occurrence is postulated to occur. The effect of neighboring channels on the flow field is taken into account by including part of them into the domain. It should be noted that variation of flow and heat transfer around a tube in a bank is determined by the flow pattern which strongly depends on the arrangement

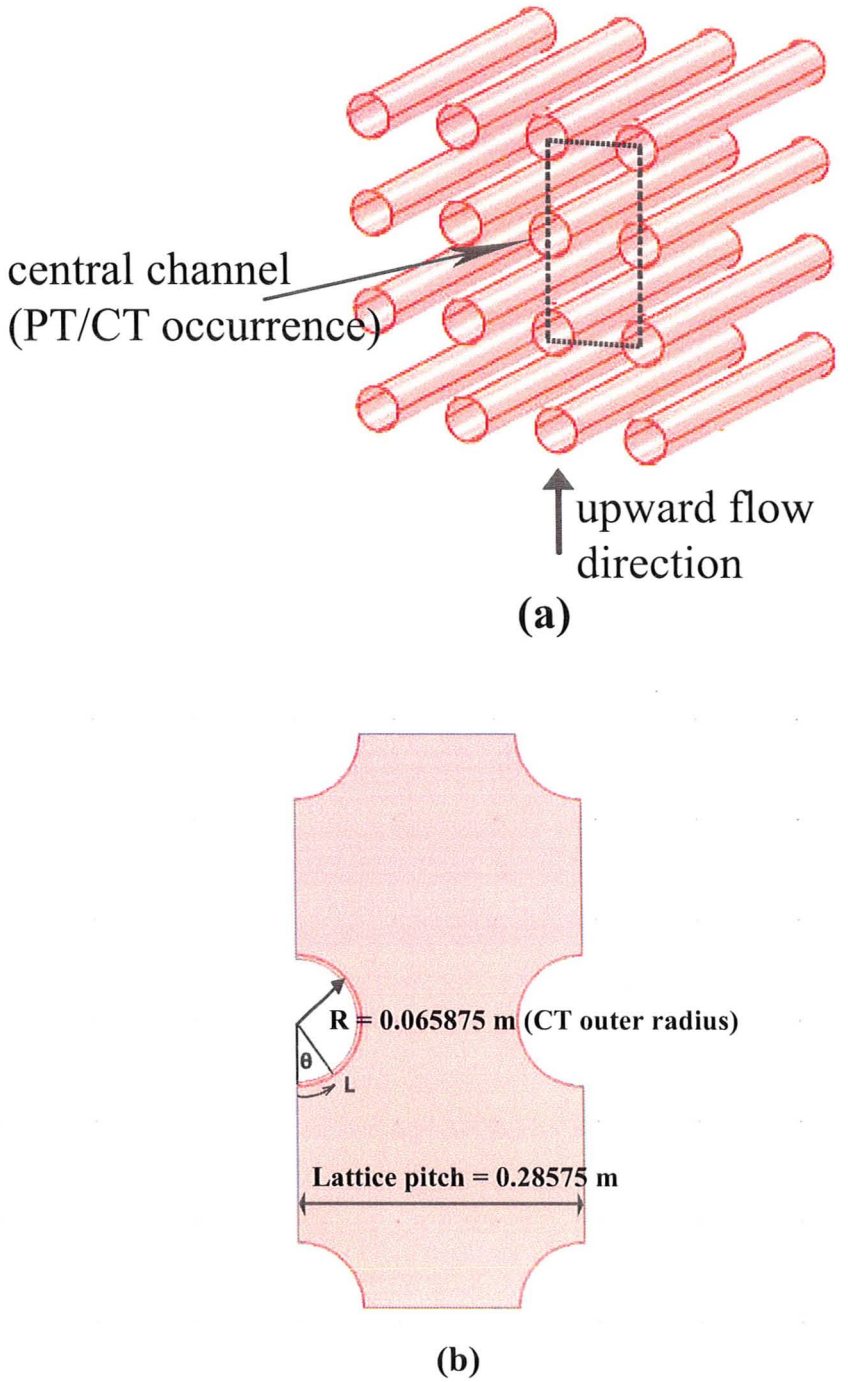

Figure 3.1: a) part of calandria tubes in 3D, b) the model geometry in 2D

of the tubes. Calandria tubes are located in an in-line tube arrangement inside the moderator. Flow around a tube in the first row is very similar to the single tube case but a tube in one of the inner rows is affected by the highly turbulent flow (Zukauskas, 1988).

3.3 Governing Equations

The standard $k-\epsilon$ turbulence model associated with a logarithmic wall function is used to predict the turbulence.

The governing equations in this model are:

- Reynolds Averaged Navier-Stokes (RANS) equations in the heavy water moderator domain:

$$\frac{D\rho}{Dt} + \rho\nabla.\mathbf{u} = 0 \tag{3.1}$$

$$\rho\frac{D\mathbf{u}}{Dt} = \mathbf{F} - \nabla p + (\mu + \mu_T)[\nabla^2\mathbf{u} + \frac{1}{3}\nabla(\nabla.\mathbf{u})] \tag{3.2}$$

- Transport equations of the turbulence models(Wilcox, 1998)

  $k-\epsilon$ **transport equations:**

$$\rho\frac{Dk}{Dt} = -\nabla.[\mu + \frac{\mu_T}{\sigma_k}\nabla k] = \frac{1}{2}\mu_T\nabla^2\mathbf{u} - \rho\epsilon \tag{3.3}$$

$$\rho\frac{D\epsilon}{Dt} - \nabla.[\mu + \frac{\mu_T}{\sigma_\epsilon}\nabla\epsilon] = \frac{1}{2}C_{\epsilon 1}\frac{\epsilon}{k}\mu_T\nabla^2\mathbf{u} - \rho C_{\epsilon 2}\frac{\epsilon^2}{k} \tag{3.4}$$

$k-\omega$ **transport equations:**

$$\rho\frac{Dk}{Dt} = -\nabla.[\mu + \mu_T\sigma_k\nabla k] + \frac{1}{2}\mu_T\nabla^2\mathbf{u} - \rho\beta_k k\omega \tag{3.5}$$

$$\rho\frac{D\omega}{Dt} = -\nabla.[\mu + \mu_T\sigma_\omega\nabla\omega] + \frac{\alpha}{2}\mu_T\frac{\omega}{k}\nabla^2\mathbf{u} - \rho\beta\omega^2 \tag{3.6}$$

- Heat transport equations in the water domain and the solid tube walls (CT thickness):

$$\rho C_p\frac{DT}{Dt} = \nabla.((\mathrm{k} + \mathrm{k}_T)\nabla T) + Q \tag{3.7}$$

Where,

$\mathbf{u}$ is the velocity field, $[m/s]$

$\mathbf{F}$ is body force, $[N/m^3]$

p is pressure, $[Pa]$

ρ is fluid density, $[kg/m^3]$

μ is dynamic viscosity, $[Pa.s]$

∇ is vector differential operator

μ_T is turbulent viscosity, $[Pa.s]$

k is the turbulent kinetic energy, $[m^2/s^2]$

ϵ is the dissipation rate of turbulence energy, $[m^2/s^3]$

k is the fluid thermal conductivity, $[W/(m.K)]$

t is time, $[s]$

k_T is turbulence thermal conductivity ($\frac{C_p \mu_T}{Pr_T}$), $[W/(m.K)]$

C_p is specific heat capacity, $[J/(kg.K)]$

Pr_T is turbulent Prandtl number

Q is the heat source, $[W/m^3]$

I is the identical matrix.

The model constants in the above equations are determined from experimental data(Wilcox, 1998); their values for $k-\epsilon$ model are: C_μ= 0.09, $C_{\epsilon 1}$= 1.44, $C_{\epsilon 2}$= 1.92, σ_k= 1.0, σ_ϵ= 1.3. The heat source is the volumetric heat flux by direct heating of neutrons, decay heat from fission products and gamma rays. Considering the total volume of heavy water in the moderator as 300 Mg and its density as 1000 kg/m^3, the volumetric heat flux can be calculated as below:

$$Q = \frac{98.7[Mw]}{300 \times 10^6[g]/1000[kg/m^3]} = 32.9 \times 10^4[W/m^3] \tag{3.8}$$

Turbulence modeling, relies on several assumptions, the most important of which are that the Reynolds number is high enough and the turbulence is in equilibrium in boundary layers, which means that production equals dissipation.

Free Convection

Free convection which is due to the density gradient, is added to the momentum balance in the body force term. This body force is $g(\rho_\infty - \rho)$, where ρ_∞ is the reference

density at the inflow temperature and ρ is the density as a function of fluid temperature.

Logarithmic Wall Function

Basically two approaches can be used for solid walls in turbulent flow. In the first approach the equations are modified by additional terms and factors in order to consider the near wall effects and the mesh size near the wall must be fine enough to resolve the viscous sublayer. Such methods are of interest for moderate Reynolds numbers, where near wall resolution leads to a reasonable number of elements . In the second approach which is used in this study a constitutive relation between the velocity and surface shear stress replaces the thin boundary layer near the wall. These relations known as wall functions are accurate for high Reynolds numbers and situations where pressure variations are not very large along the wall. The idea of the wall functions approach (Launder and Spalding, 1972) is to apply boundary conditions some distance δ_W away from the actual wall, so that the turbulence model equations are not solved close to the wall. The flow is considered to be parallel to the wall. In order to explain the logarithmic wall functions some definitions are briefly introduced. Close to the wall the fluid viscosity ν and the wall shear stress τ_w are important parameters. from these quantities and also the fluid density ρ, we define appropriate velocity and lengthscale in the near wall region denoted as u_τ and l^* respectively. These quantities are defined as:

$$u_\tau = \sqrt{\frac{\tau_w}{\rho}} \tag{3.9}$$

$$l^* = \frac{\mu}{\rho u_\tau} \tag{3.10}$$

Later on we define δ_w^+ which is the distance from the wall normalized by the viscous lengthscale l^* and is given by

$$\delta_w^+ = \frac{\delta_w}{l^*} = \frac{u_\tau \delta_w}{\nu} \tag{3.11}$$

where $\nu = \mu/\rho$ is the kinematic viscosity.

The logarithmic wall functions are formally valid for values of δ_w^+ between 30 and 100. Because the wall function assumes that the flow is parallel to the wall, the velocity component perpendicular to the wall is zero.

Referring to the logarithmic law of the wall (Von Karman, 1930) the velocity can be described by

$$\bar{\mathbf{u}}^+ = \frac{\bar{\mathbf{u}}}{u_\tau} = \frac{1}{\kappa} \ln(\delta_w^+) + C^+ \tag{3.12}$$

where $\bar{\mathbf{u}}^+$ is the mean velocity normalized by the friction velocity, κ denotes the Von Karman's constant (about 0.41) and C^+ is a universal constant (about 5.2 for smooth walls) (Schlichting, 2000).

Thermal Wall Function

In order to model the temperature in the laminar boundary layer at the CT/liquid interface, a thermal wall function Equation (3.13) is applied which relates the resistance to heat transfer through the laminar boundary layer to that for momentum transfer for the fluid. The heat flux is determined by: (COMSOL, 2008)

$$q = \frac{\rho C_p C_\mu^{0.25} k_w^{0.5} (T_w - T)}{T^+} \tag{3.13}$$

where, ρ and C_p are the fluid density and specific heat capacity, respectively, C_μ is a numerical constant of the turbulence model, and k_w is the turbulent kinematic energy at the wall. Furthermore, T_w is the wall temperature while T is the fluid temperature. The quantity T^+ is related to the wall offset in viscous units, δ_w^+, through the definition:

$$T^+ = \frac{Pr_T}{\kappa} ln(\delta_w^+) + \beta \tag{3.14}$$

where the turbulent Prandtl number Pr_T is fixed to 0.85 (Kays, 1994), the von Karman constant κ obtained from experiments is equal to 0.41 (Schlichting, 2000). β is a model constant set to 3.27 (Kays, 1994). The wall offset in viscous units is defined as:

$$\delta_w^+ = \frac{\delta_w C_\mu^{0.25} k_w^{0.5}}{\nu} \tag{3.15}$$

where, δ_w is specified wall offset which is considered as half the local mesh size at the boundary.

The above equations are solved simultaneously inside the domain shown in Figure 3.1-b using finite element method(Zienkiewicz, 2005) in order to find the unknowns $(\bar{\mathbf{u}}(u,v), p, T, k, \epsilon)$. The number of elements is 6230 with an unstructured mesh in accordance with the mesh sensitivity analysis describing in section 3.6. The number of degree of freedom is 58062.

3.4 Material Properties

Physical properties of water as a function of temperature are implemented from XSteam (Holmgren, 2007) into the model. These functions consist of water specific heat capacity, thermal conductivity, dynamic viscosity and density are shown in Figure 3.2 to 3.5 respectively.

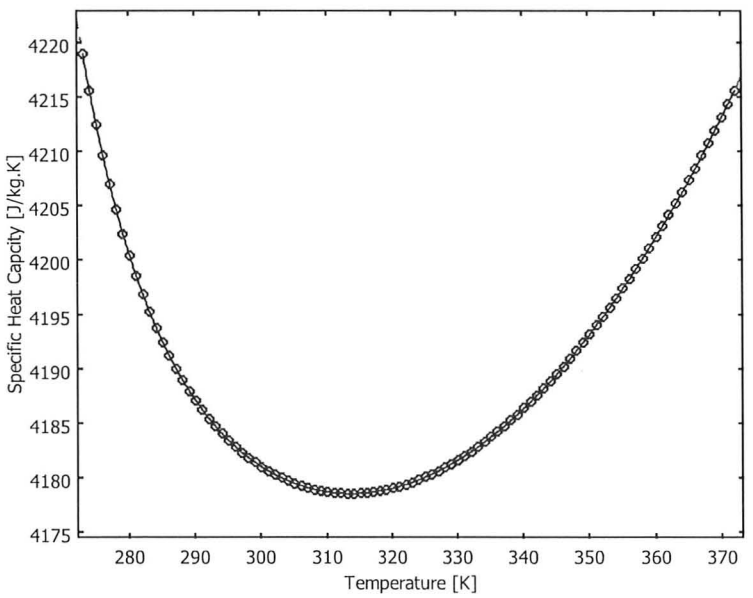

Figure 3.2: Water specific heat capacity

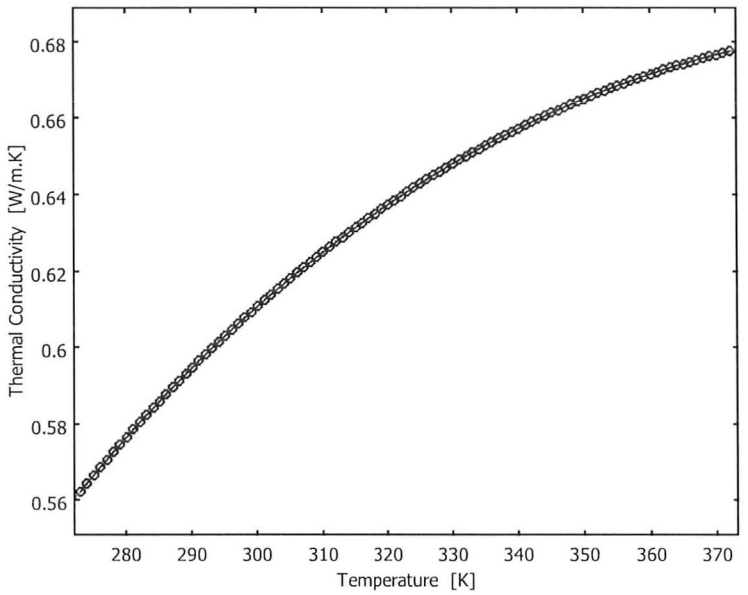

Figure 3.3: Water thermal conductivity

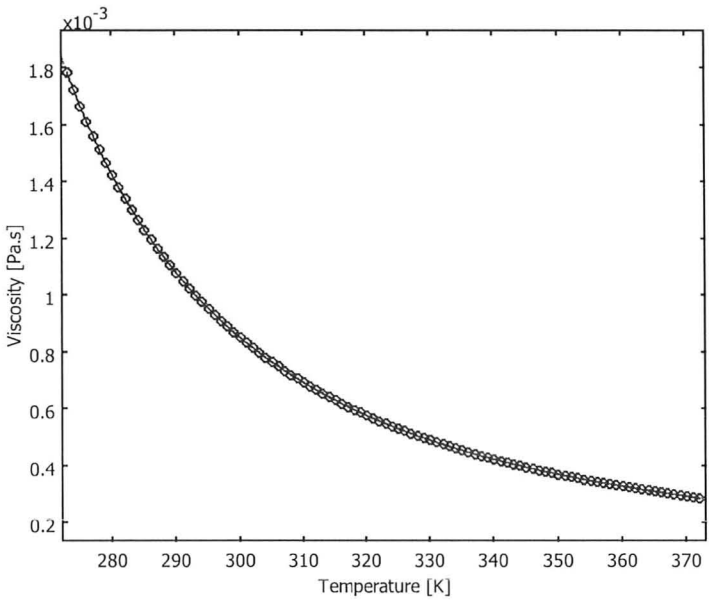

Figure 3.4: Water dynamic viscosity

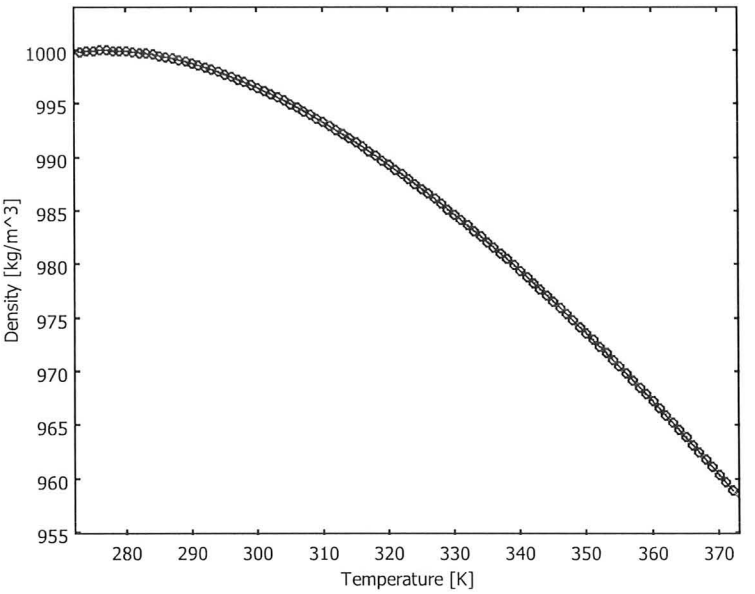

Figure 3.5: Water density

Material properties of zircaloy as a function of temperature are taken from the MatPRO (1993). These functions are shown in Figure 3.6 and 3.7.

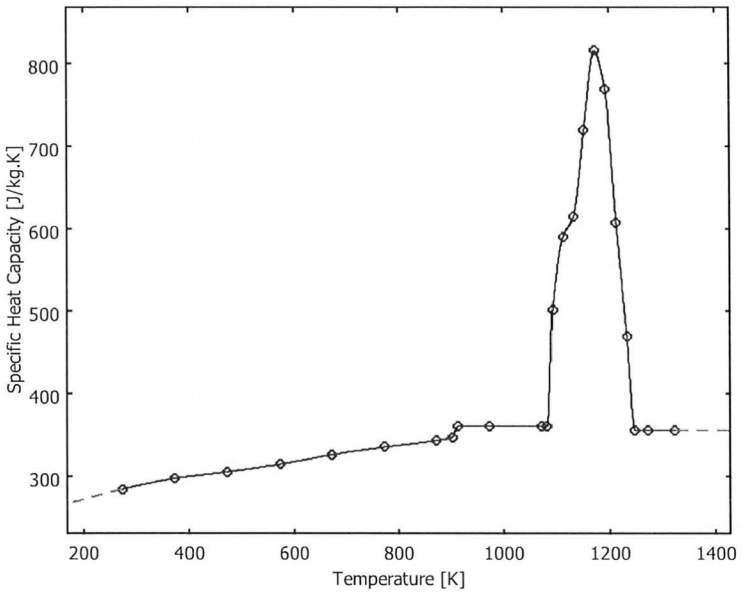

Figure 3.6: Zircaloy specific heat capacity

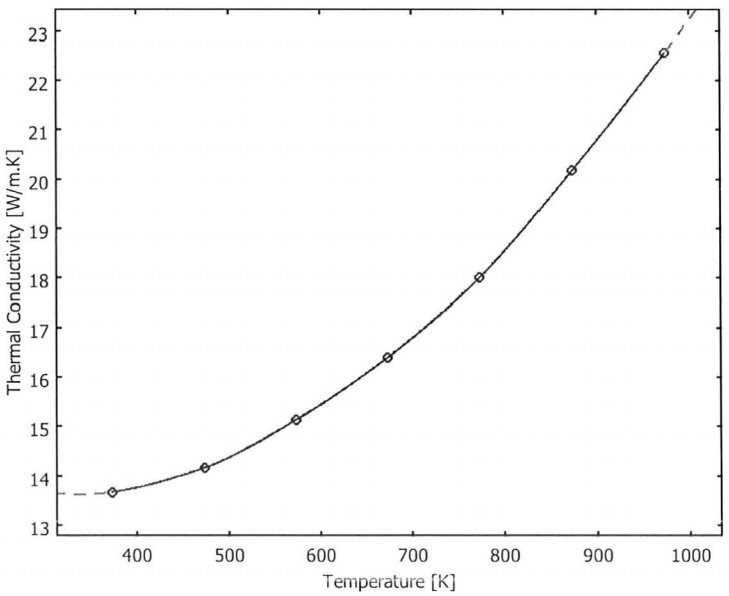

Figure 3.7: Zircaloy thermal conductivity

3.5 boundary conditions

Two groups of boundary conditions are applied to the model, one group is for the $k-\epsilon$ Equations (3.1) to (3.4) in the fluid domain and the other group is for the heat transport Equation (3.3).

3.5.1 Navier-Stokes Equations

For Navier-Stokes equations in the fluid domain the specified boundary conditions are:

- A pressure difference between inlet and outlet given by the mass flow.
- Normal flow and stream-wise periodic conditions for velocity, at the inlet and outlet.
- Symmetry boundary condition at the region borders.

3.5.2 Heat Transport Equation

For the heat transport equation, the boundary conditions are specifies as:

- Moderator temperature with different subcoolings at the inlet.
- Convection dominated transport at the outlet of the domain.
- At the inner surface of calandria tubes a heat flux associated with normal operation is implemented. While, in central one after a postulated PT/CT contact, the applied heat flux is increased with time until the saturation point is reached in the fluid.

- The borders of the domain are considered to be symmetric.

3.6 Mesh Effect

In order to compute turbulent flows successfully, some consideration is needed during the mesh generation. Turbulence through the spatially-varying effective viscosity plays an important role in the transport of mean momentum and other parameters. Therefore, in order to obtain more accurate results it is important to make sure that turbulence quantities in complex turbulent flows are properly resolved. The fluid velocity, the heat transfer coefficient and consequently the temperature at the boundaries are very sensitive to the number of mesh. The logarithmic wall function in section 3.5 is valid under certain conditions that depend on the resolution, the velocity and the viscosity. The wall function uses the dimensionless wall offset which for the first internal node should be less than some upper limit dependent on the Reynolds number.

Figure 3.8 depicts the wall offset parameter versus the CT surface arc-length for two different velocities. Referring to the Figure 3.1- b, zero arc-length indicates the arc-length of the lowest point of the cylinder in the geometry ($\theta = 0°$) and arc-length equal to 0.21 indicates the top of the cylinder ($\theta = 180°$). As can be seen in Figure 3.8 the dimensionless wall offset is changing along the surface depending on the velocity at the wall. δ_w^+ is larger at higher velocities than the lower velocities. For the wall function to be an accurate approximation, δ_w^+ for the first internal node should be larger than 30 but less than 100. For high Reynolds number, the upper limit can be extended to a few hundred (COMSOL, 2008). From Equation (3.11) one can conclude

that δ_w^+ depends on the specified wall offset which in this model is considered as half of the local mesh size at the boundary, the fluid kinematic viscosity and the velocity at the wall. The changes in kinematic viscosity is very small, therefore, to have an accurate wall function approximation by increasing the velocity at the boundary, the mesh size needs to be reduced to avoid δ_w^+ become more than the higher limit. In order to reach to this value the number of mesh at the boundary has been made fine enough to satisfy this condition and to get accurate fluid velocity and heat transfer coefficient at the CT surface. Eventually, maximum applied mesh size on the central CT surface is about 1mm to have an accurate wall function for our modeling.

In Figure 3.9 the mesh distribution in the domain is shown. It can be seen that the mesh resolution on the cylinder surface where we applied the logarithmic wall function, is much higher than the other regions. The mesh size was made small enough until no significant change was observed in the results by further refinement.

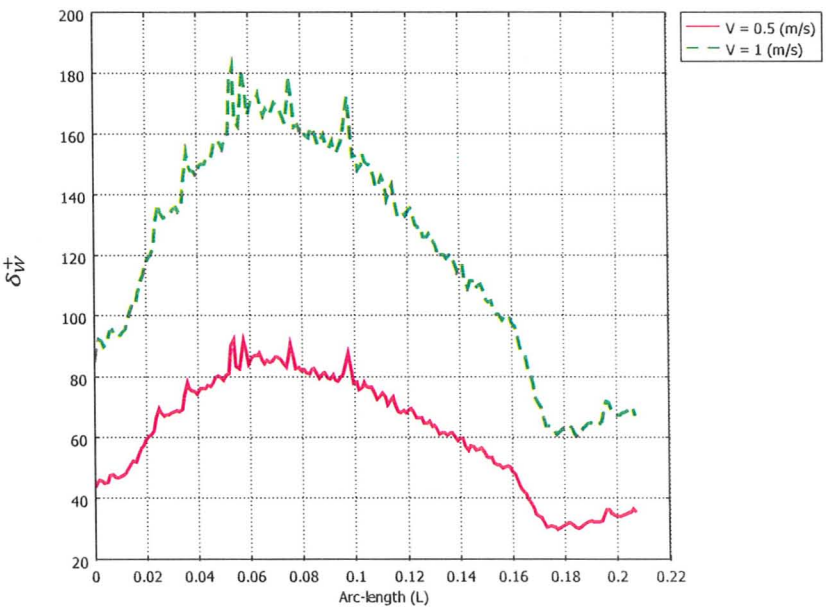

Figure 3.8: Wall offset in viscous units at the CT surface

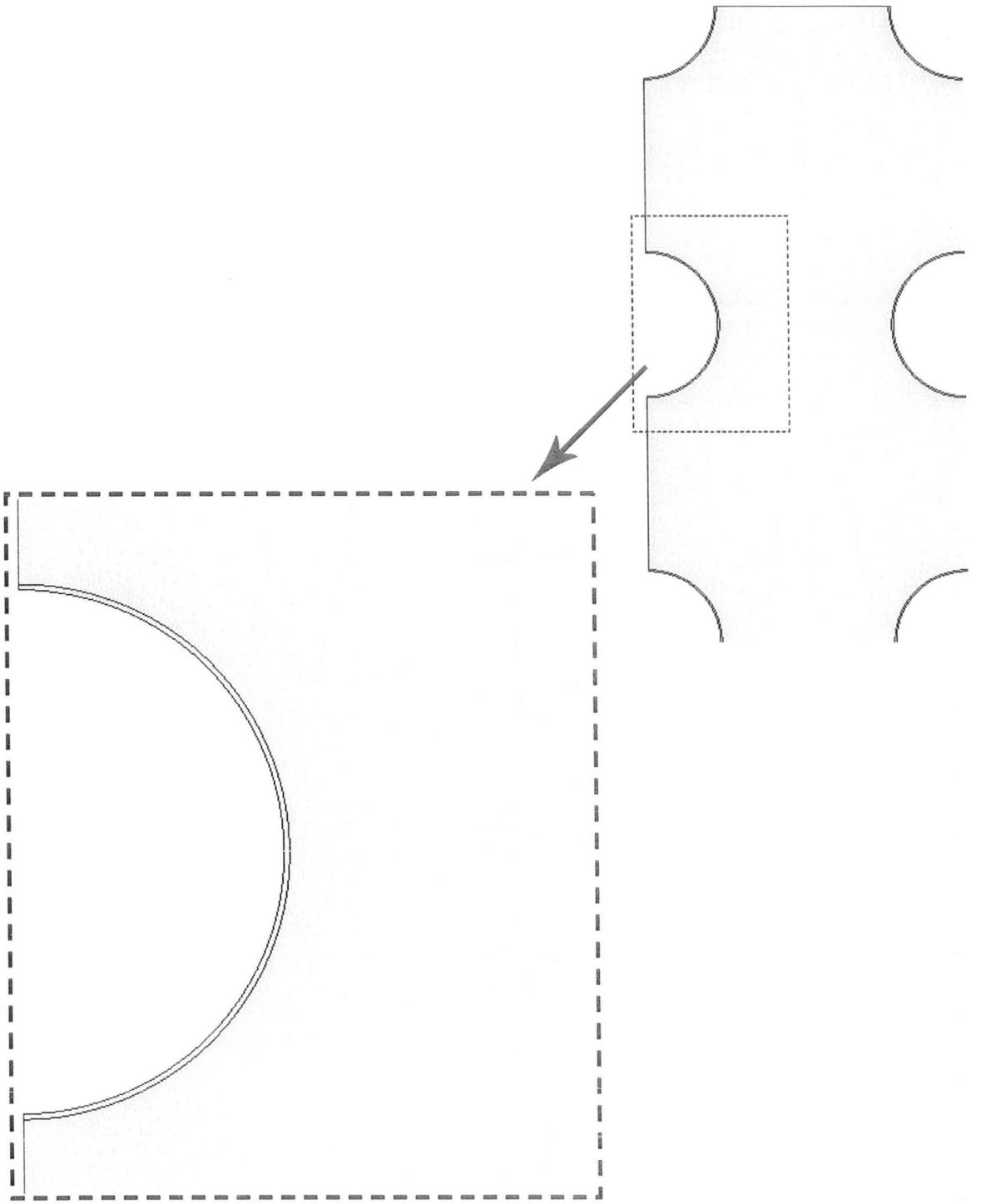

Figure 3.9: Mesh

Chapter 4

Results and Discussion

The main objective of this study is to determine the nature of the temperature fluctuations and the interplay of velocity and temperature field in the vicinity of the calandria tubes after PT/CT contact. In this chapter the results will be described and discussed for $k-\epsilon$ and $k-\omega$ turbulent models separately. The results of these two different models are compared for both buoyancy dominated (upward) flow and momentum dominated (downward) flow. The model considers the steady state solution as initial value for the transient condition. The figures shown in this chapter for transient case describe the conditions around the central CT (see Figure 3.1) at 1 second after PT/CT contact.

4.1 Steady-Sate Results

To obtained the initial values for the transient case, a steady-state problem has been solved first. In the steady-state case all six channels are in the normal operation. Figure 4.1 shows the velocity streamlines in the domain. Red color is associated with

high velocity regions, while, blue indicates the low velocity regions. From the velocity distribution one can conclude that fluid velocity is low at the top and at the bottom of the CTs. The flow field is periodic in the y direction. It is also shown that the velocity field in the domain is symmetric.

Figure4.2 shows the velocity contours using periodic velocity conditions. It can be seen that the inflow and outflow velocity profiles match. It also shows the velocity profile at the inflow region.

4.2 $k - \epsilon$ model

Figure 4.3 shows the local pressure and velocity variations in the condition that fluid enters the domain from the bottom with $1m/s$ velocity and $20°C$ subcooling. In this condition the Reynolds number is around 65000. The Figure indicates the opposite behavior of velocity and pressure on the cylinder. From $\mathbf{u} = 0$ at the stagnation point ($\theta = 0$), the fluid accelerates due to the pressure gradient ($d\mathbf{u}/dL > 0$ when $dp/dL < 0$), reaches to a maximum velocity when $dp/dL = 0$ and decelerates as a result of the adverse pressure gradient ($d\mathbf{u}/dL < 0$ when $dp/dL > 0$). As was mentioned before referring to the Figure 3.1-b, L denotes the arc-length and θ is its associated angle. Eventually the sign of velocity gradients changes and velocity becomes zero at the separation point where the boundary layer detaches from the surface and a wake is formed in the downstream region (see Figure 4.4). This is the point at which the energy in the flow is insufficient to overcome the increasing pressure and the flow separates from the surface. The predicted flow behavior in this model is in very good agreement with the flow profile normal to circular cylinder described by Incropera

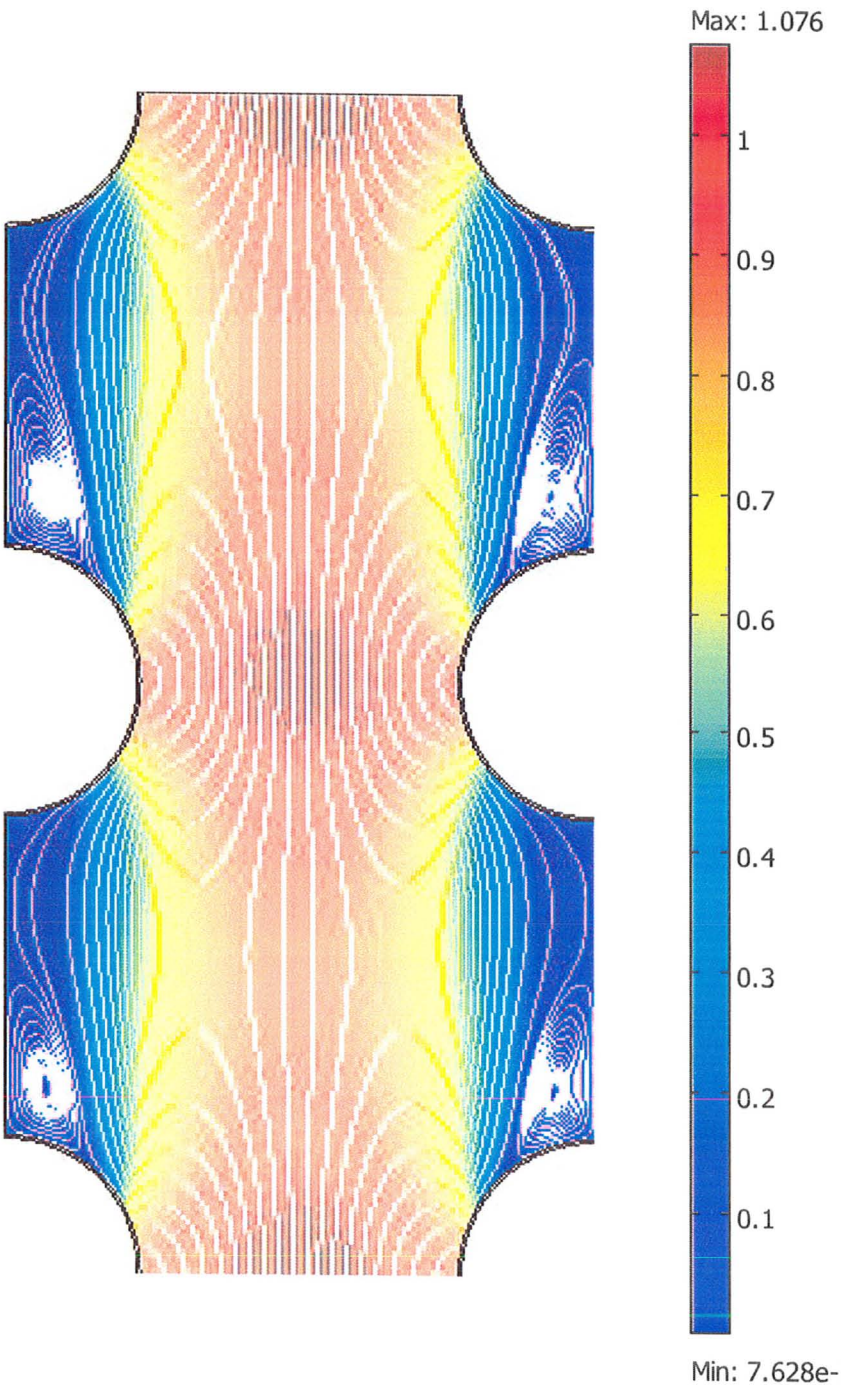

Figure 4.1: Velocity streamlines in the steady-state case for upward flow

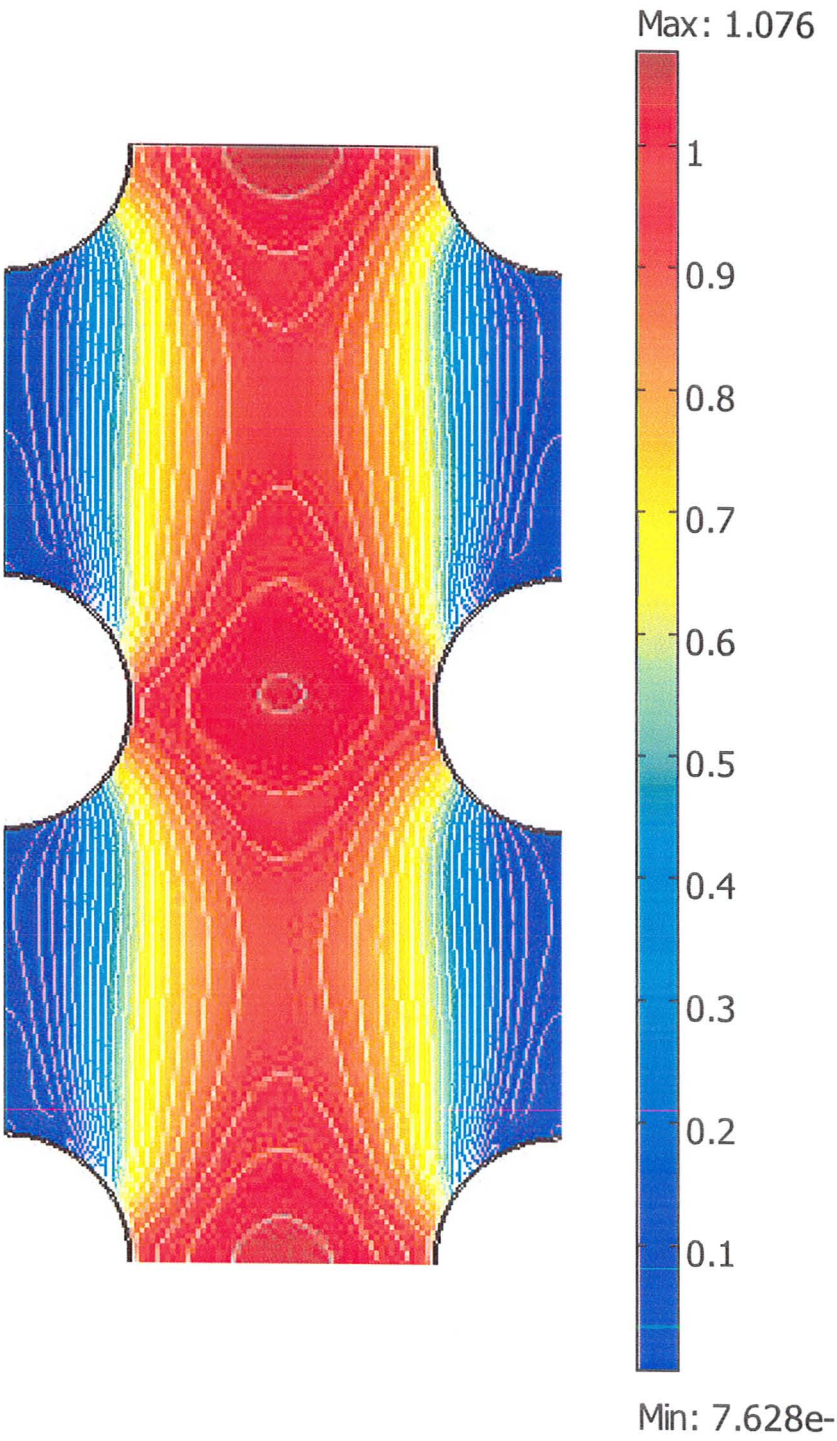

Figure 4.2: Velocity contours in the steady-state case for upward flow

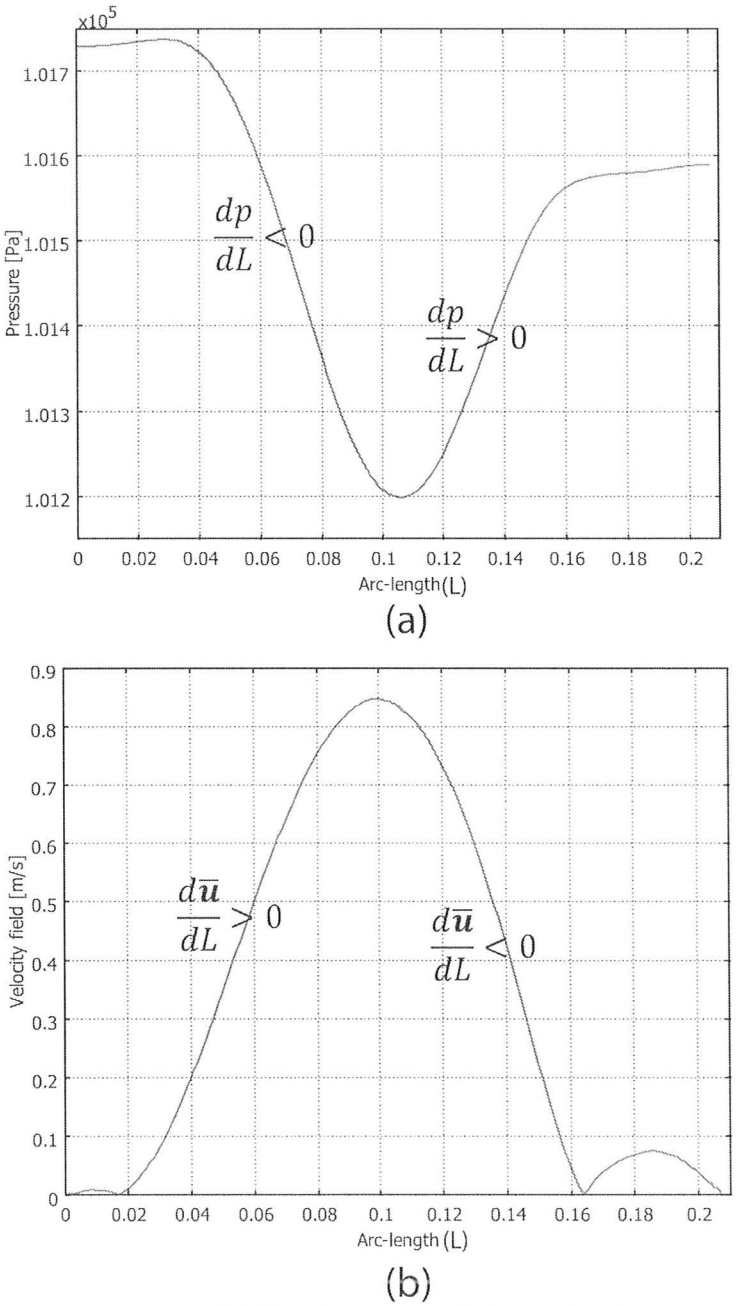

Figure 4.3: (a) Local pressure (b) Local velocity

(1990). It is seen from the Figure 4.3-a that the pressure is at a maximum at the stagnation point and at a minimum at the central section. For an ideal fluid, the pressure distribution would be symmetrically and the pressure integration results in a zero value for the force on the cylinder. However, for real fluids as indicated in Figure 4.3-a, the nonsymmetrical pressure distribution results to a net force on the cylinder. This force is the main cause of the pressure drop across the cylinder.

Figure 4.4 shows the temperature distribution and velocity streamlines for an inlet flow velocity of $0.5m/s$ for both upward and downward flow. Arrows indicate the flow direction while the colors show the temperature distribution. Three different areas for the velocity field can be clearly seen:

- The stagnation point in the front
- The recirculation zone in the rear behind the cylinder
- High velocity regions in the middle of the cylinder

It is important to note that the heat transfer is strongly influenced by the details of the velocity field.

Figure 4.5 shows the velocity versus arc-length on the surface of the central CT after contact for upward and downward flows. The velocities in x and y direction are plotted separately and it is evident that the velocity in both directions is zero at the stagnation region ($L = [0 - 0.02]$ for upward flow and $L = [0.19 - 0.21]$ for downward flow) and this indicates that if boiling occurs, accumulation of vapor bubbles may produce a stable vapor film at this region which will reduce the local heat transfer

coefficient. This can cause overheating of the CT surface and affect channel integrity if the vapor film extends around the tube. As a sensitivity analysis, different cases have been analyzed with different subcoolings and similar behavior was observed.

The separation of the boundary layer from the cylinder surface is an important factor in determining a number of processes such as pressure drop, velocity distribution near the surface and in the external layers, flow in the wake, etc. The position of the separation point is strongly dependent on the Reynolds number. For laminar flows as a result of viscous forces, the separation point is generally at the rear end. By increasing the Reynolds number, effect of inertia forces increases and this creates a turbulent boundary layer. Larger momentum of fluid in the turbulent boundary layer leads to delay of the separation point. It is observed in this study that the separation point occurs at $L \simeq 0.16$ or $\theta = 137$ degree, which is very close to the experimental as well as theoretical value of $\theta = 140$ degree (Incropera, 1990; Zukauskas, 1985).

Temperature distribution of the fluid around the central CT is shown in Figure 4.6 for different subcoolings of upward flow. Maximum temperature in the fluid is considered to be less than saturation. For each subcooling starting at the stagnation point $\theta = 0$ and $L = 0$, temperature decreases with increasing arc-length due to increase in velocity and heat transfer coefficient. However by developing the laminar boundary layer on the CT surface, the heat transfer coefficient decreases and temperature increases to its maximum value considered in this model. Eventually, separation occurs at $L = 0.16$ and fluid temperature declines due to the increase in heat transfer coefficient as a result of the considerable mixing associated with the wake region. However,

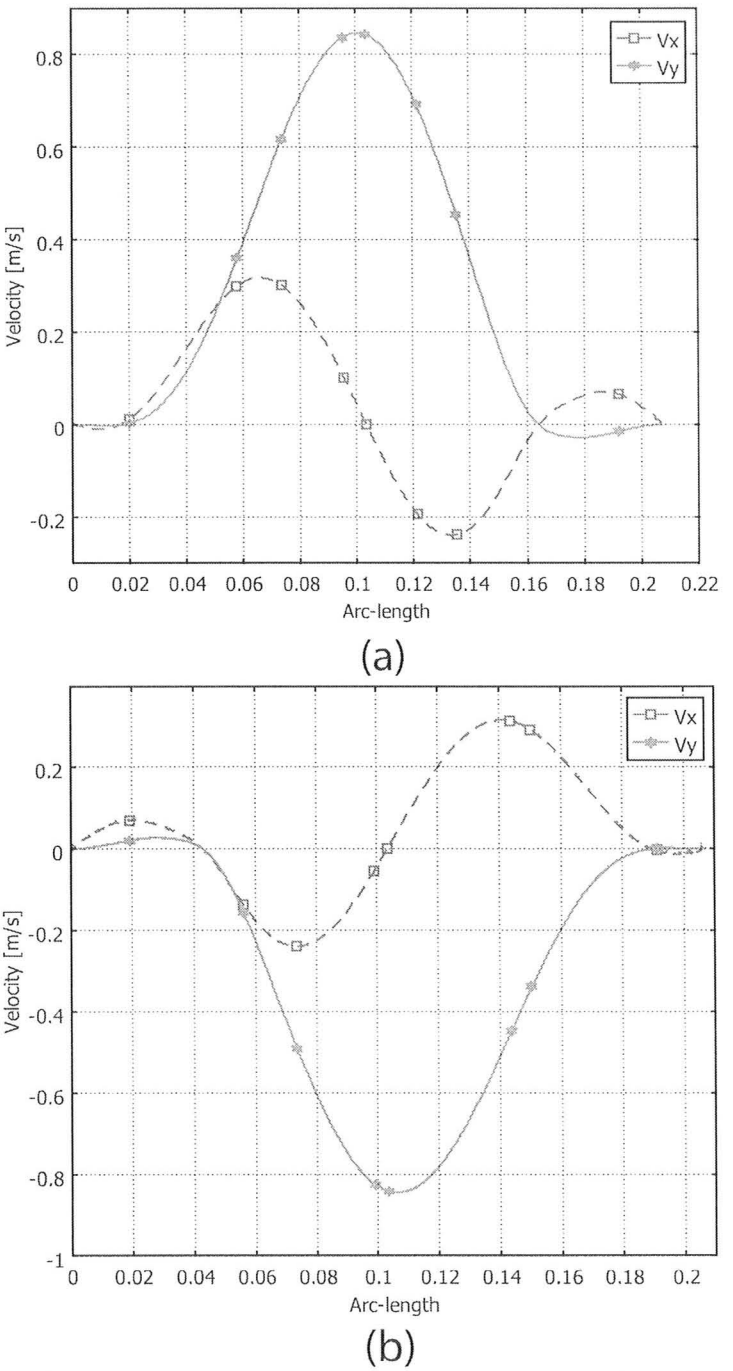

Figure 4.5: Velocity field around the CT for a) upward and b) downward flows

as can be observed in the Figure 4.6 the variations in local fluid temperature become smaller as subcooling reduces. Qualitatively, this indicates a greater tendency for vapor film to extend around the CT surface as subcooling decreases. This signifies the importance of moderator fluid subcooling in the situation of critical break LOCA inside the CANDU reactor. As subcooling increases the region of high fluid temperature become increasingly localized which will result in higher likelihood of quenching. This makes the spreading of drypatches around the CT more difficult.

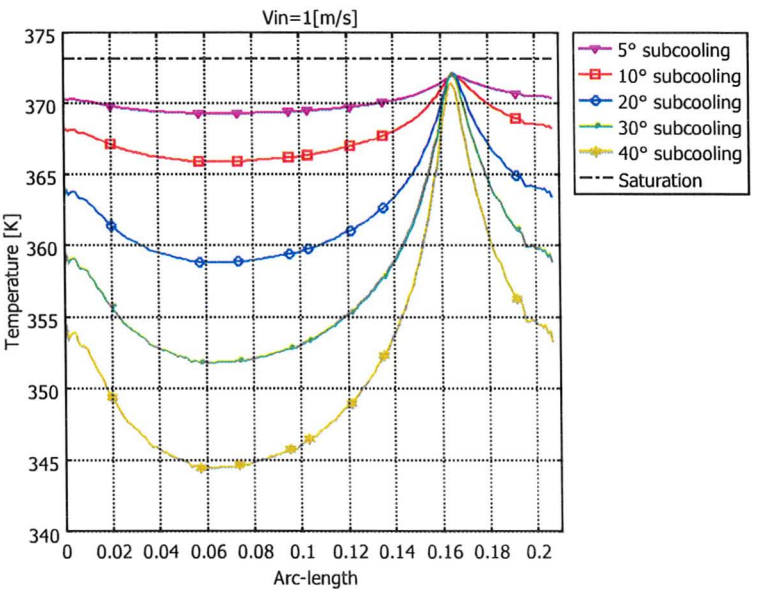

Figure 4.6: Local temperature around CT for upward flow by $k - \epsilon$ model

Figure 4.7 shows the temperature distribution around the central CT for downward flow with different subcoolings. Similar to the upward flow, the maximum fluid temperature is considered to be less than the saturation point. The same behavior

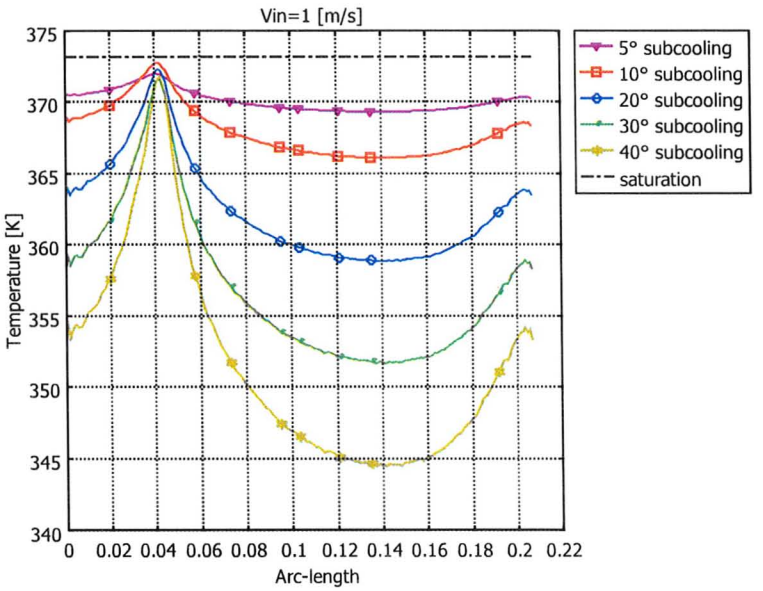

Figure 4.7: Local temperature around CT for downward flow by $k - \epsilon$ model

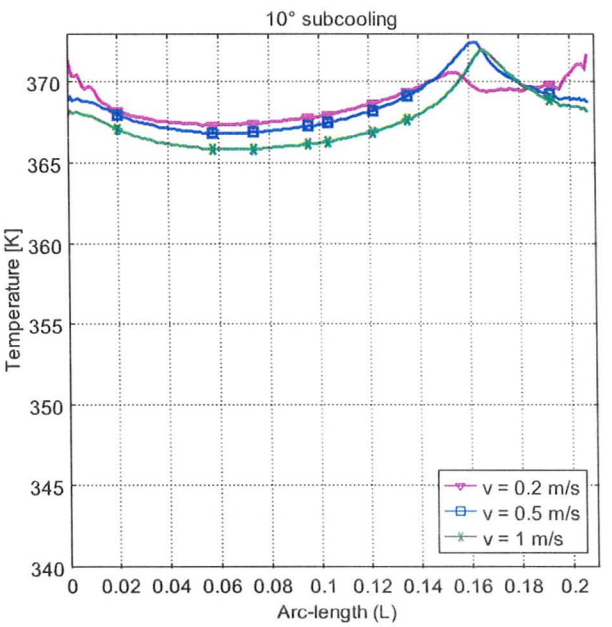

Figure 4.8: Local temperature for different velocities in upward flow, $k - \epsilon$ model

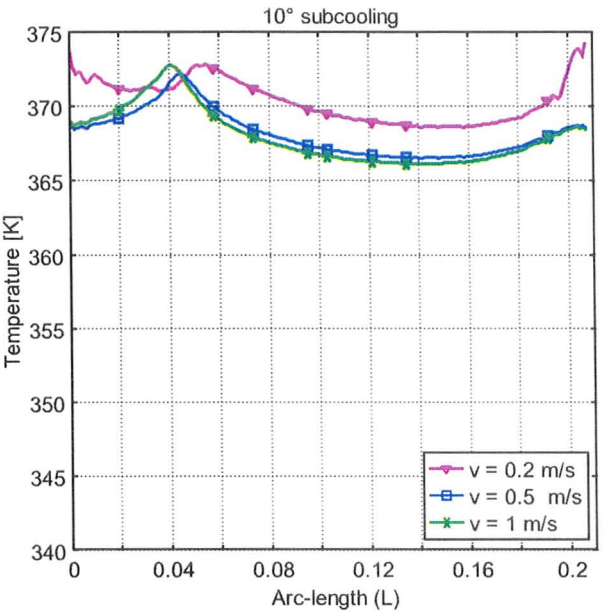

Figure 4.9: Local temperature for different velocities in downward flow, $k - \epsilon$ model

as the upward flow can be seen in the downward situation. As it is shown in Figure 4.7 for each subcooling starting from the stagnation point which is at $\theta = 180$ and $L = 0.21$, due to the increase in fluid velocity and heat transfer coefficient, temperature decreases. By developing the laminar boundary layer, the heat transfer coefficient decreases and temperature increases to its maximum value. After the separation point around $L = 0.04$ due to the increase in heat transfer coefficient in the wake region, fluid temperature decreases. Similar to the upward flow again it should be noted that as subcooling decreases, the variations in local fluid temperature become smaller and therefore it is more probable for the vapor film to extend around the CT surface at low subcoolings.

As a sensitivity analysis and in order to show the effect of inlet velocity, Figures 4.8

and 4.9 indicate the local temperature variations for different inlet velocities at 10^o subcooling for upward and downward flow, respectively. From these figures obtained with $k-\epsilon$ model, it can be seen that by decreasing the inlet velocity, the overall temperature becomes higher especially in downward flow. This can be explained by the buoyancy force acting on the fluid. In upward flow, since the buoyancy acts on the same direction as the fluid flow, no significant change was observed for different inlet velocities. But in downward flow, due to the opposite direction of the buoyancy force and fluid flow, buoyancy effects become more effective, specially at lower fluid velocities.

Density variations for upward flow are shown in Figure 4.10. As the fluid heats up the density decreases and the velocity slightly increases. Thus, the boundary layer decreases and the local heat transfer coefficient should become larger. Neglecting the density variations in the model results in underestimation of the cooling/heating power. This points out the importance of taking density variations into account. Although the temperature gradient results to density variations inside the fluid, no major difference was observed between the upward and downward flows behavior. However we expect that if boiling occurs, due to the large change in the fluid density, buoyancy forces affect the flow behavior for upward and downward flows significantly.

Figure 4.11 shows the local heat transfer coefficient around the central CT for different inlet velocities of upward flow, obtained by $k-\epsilon$ model. As it was mentioned before, due to the highly complicated structure of fluid dynamics, various regions exist on the cylinder surface. The laminar boundary layer on the front part of the

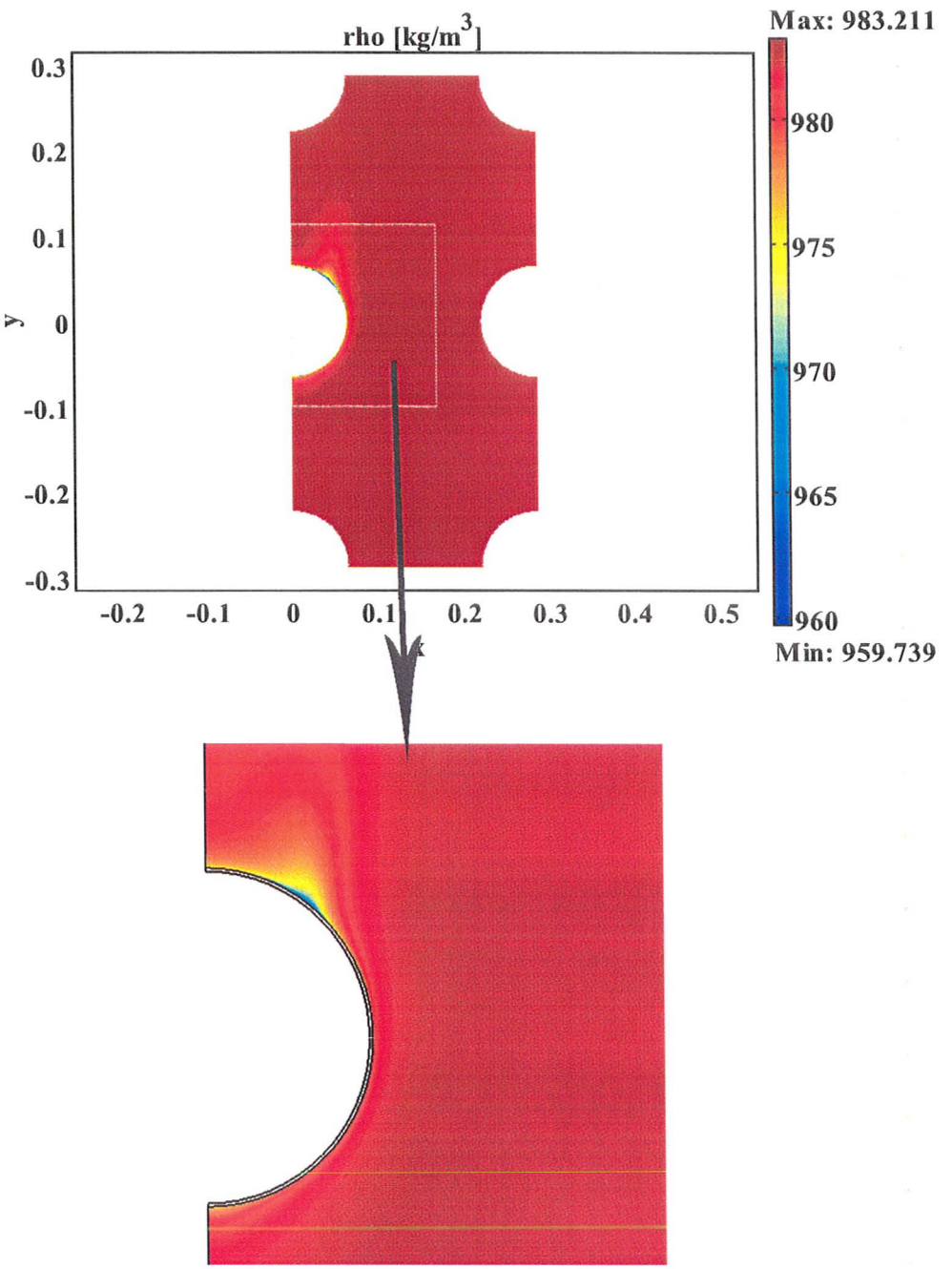

Figure 4.10: Fluid density in the domain (upward flow)

cylinder can become partially turbulent under certain conditions. Laminar-turbulent transition in the boundary layer and boundary layer separation are governed by the Reynolds number. Vortex flow occurs in the rear of the cylinder. Due to different fluid dynamics, the two stagnation points (one in the front and one in the rear) must be treated separately. Therefore the heat transfer on the cylinder surface is a complex character and it is important to determine the local heat transfer coefficient. Increasing Reynolds number causes an increase in heat transfer due to the thinning of the laminar boundary layer. As shown in Figure 4.11 at higher velocities the local heat transfer becomes larger over the whole cylinder surface (From $\theta = 0$ and $L = 0$ to $\theta = 180$ and $L = 0.21$). No essential change can be seen in the distribution profile of the heat transfer coefficient in these results. As the figure shows, starting from the stagnation point in the front of the cylinder ($\theta = 0$ and $L = 0$), heat transfer coefficient increases appreciably. This is associated with high acceleration of the flow in the frontal side of the tube. The interactions from tubes in neighboring lines should also be considered. In fact the shear layer separated from the lower cylinder attaches around $\theta \simeq 60$ and $L \simeq 0.07$ and consequently the heat transfer coefficient reaches to a maximum value. After that heat transfer coefficient decreases because of the large thickness of thermal boundary layer creating thermal resistance. In the rear side of the cylinder, the level and character of the local heat transfer coefficient depends on the intensity of circulation. Separation of the boundary layer causes an increase in the heat transfer coefficient in the rear side of the cylinder starting from $\theta \simeq 154^{\circ}$ and $L \simeq 0.18$.

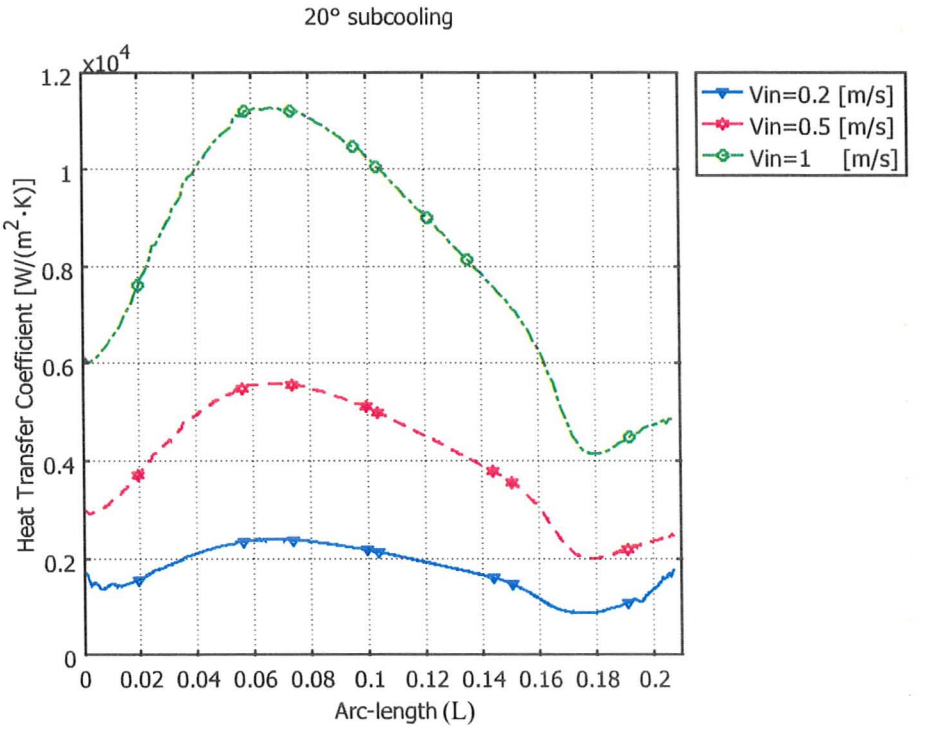

Figure 4.11: HTC around CT for different inlet velocities for upward flow by $k-\epsilon$

4.3 $k-\omega$ model

Figure 4.12 shows the temperature distribution and velocity streamlines in the domain for both upward and downward flow obtained by the $k-\omega$ model. It can be seen that in $k-\omega$ predictions, the wake region on the cylinder is larger than previous model.

Figure 4.13 shows the local pressure and velocity variations obtained by $k-\omega$ model when flow enters the domain at $20°C$ subcooling with velocity of $1m/s$. The opposite behavior of pressure and velocity can be seen similar to the $k-\epsilon$ results.

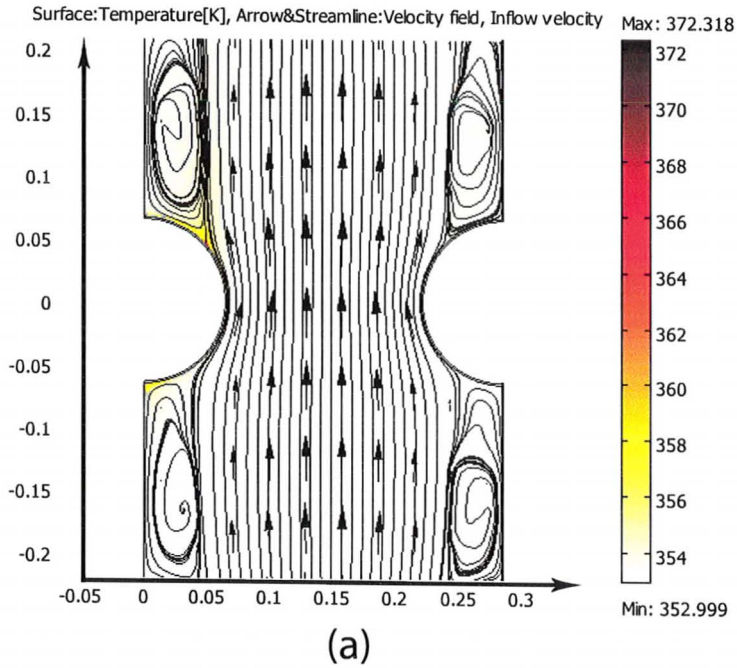

Figure 4.12: Velocity streamlines for upward and downward flows, $k-\omega$ model

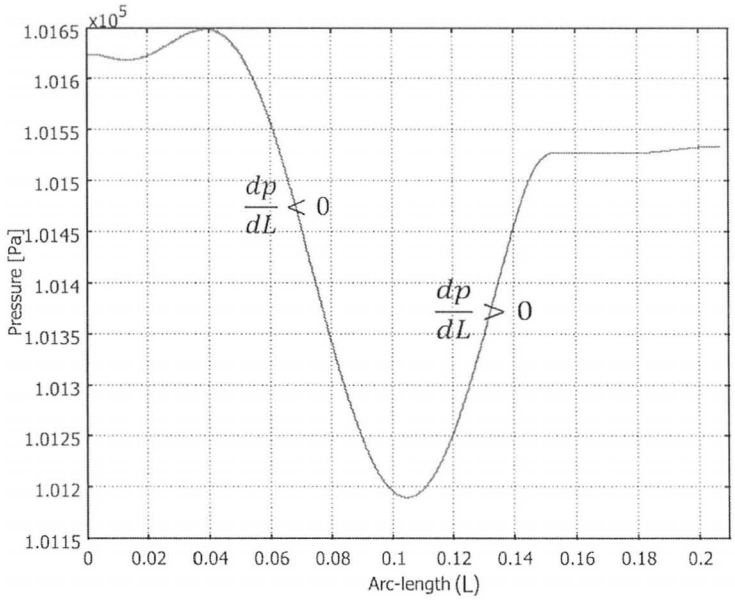

(a)

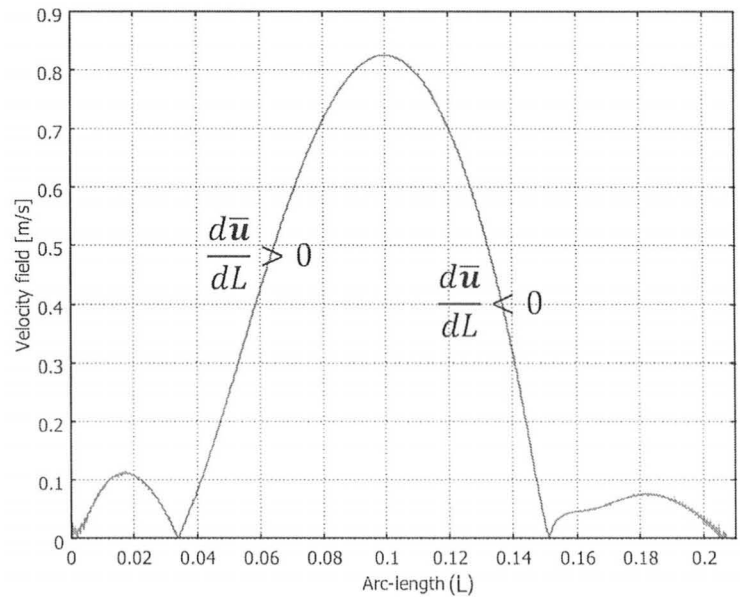

(b)

Figure 4.13: (a) Local pressure (b) Local velocity, $k - \omega$ model

Figure 4.14 shows the velocity components around the cylinder obtained by $k-\omega$ model for both upward and downward flows. The velocity components at the stagnation regions in the front and in the rear of the cylinder are indicated. Although the velocity components in these regions are not zero but they have a very small value compare to the other parts of the cylinder.

Temperature distribution around the central CT for different subcoolings obtained by $k-\omega$ model is shown in Figures 4.15 and 4.16 for upward and downward flows respectively. Maximum temperature in the fluid is considered to be less than saturation. The same as the $k-\epsilon$ model for each subcooling starting at the stagnation point ($\theta = 0$ and $L = 0$ for upward flow and $\theta = 180$ and $L = 0.21$ for downward flow, temperature decreases with increasing arc-length due to increase in velocity and heat transfer coefficient. By developing the laminar boundary layer on the CT surface, the heat transfer coefficient decreases and temperature increases. Eventually, separation occurs at $L \simeq 0.15$ and fluid temperature declines due to the increase in heat transfer coefficient in the wake region. As can be observed from the $k-\omega$ results, the variations in local fluid temperature become smaller as subcooling reduces. Qualitatively, this indicates a greater tendency for vapor film to extend around the CT surface as subcooling decreases.

As a sensitivity analysis and in order to show the effect of inlet velocity, Figures 4.17 and 4.18 indicate the local temperature variations for different inlet velocities at 10^o subcooling for upward and downward flow, respectively. From these figures obtained by $k-\omega$ model, it can be seen that by decreasing the inlet velocity,

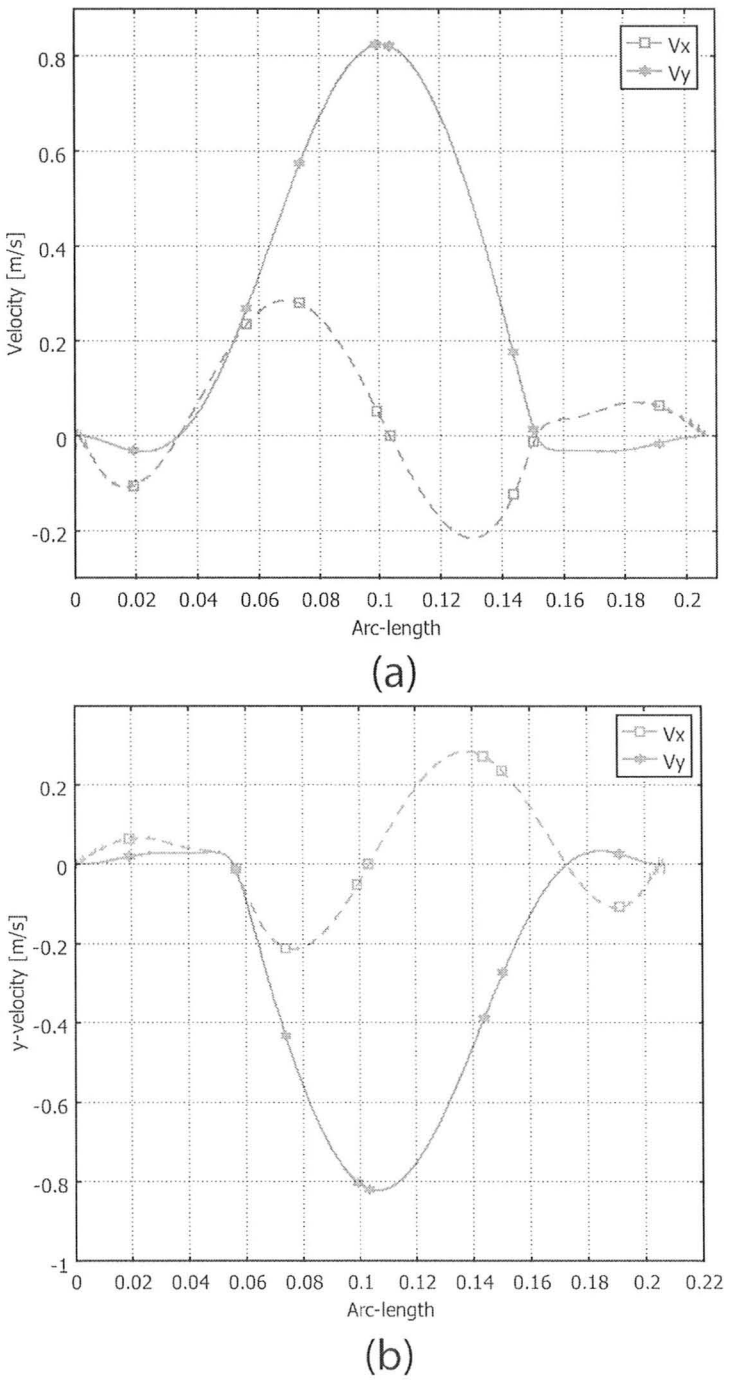

Figure 4.14: Velocity field (a) upward flow, (b) downward flow, $k - \omega$ model

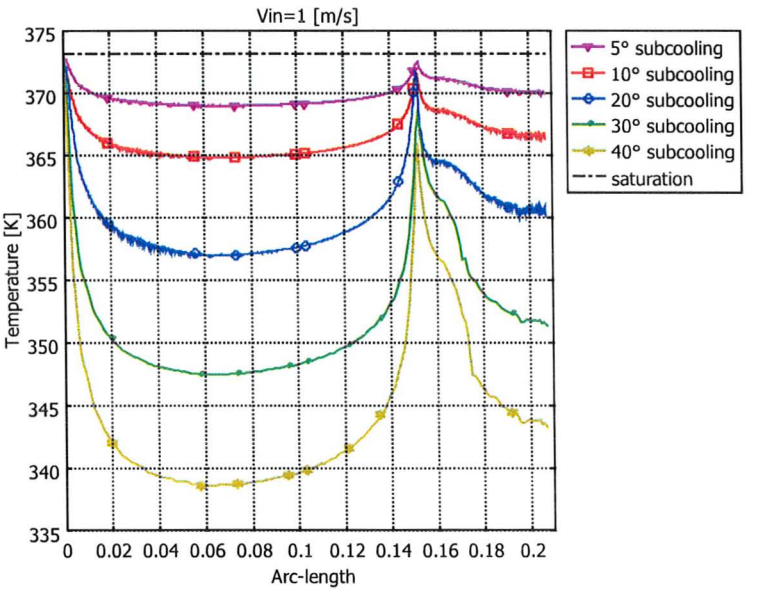

Figure 4.15: Local temperature around CT for upward flow by $k-\omega$ model

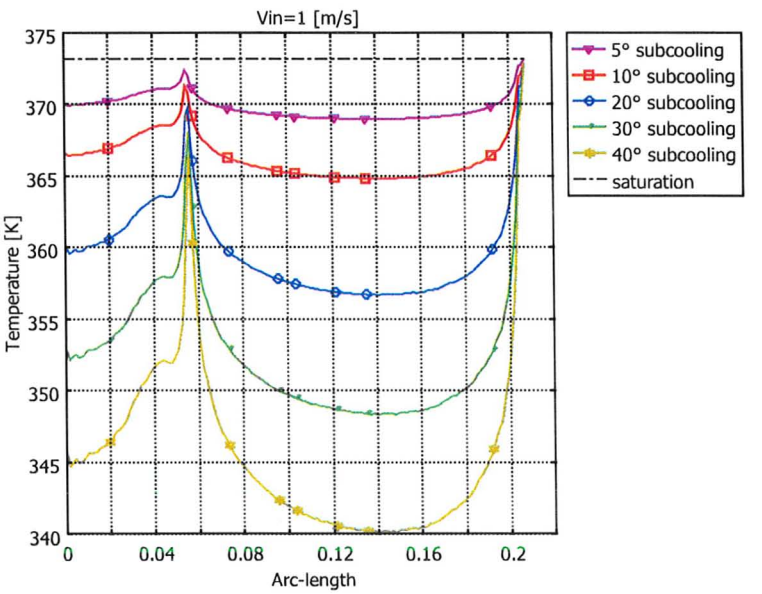

Figure 4.16: Local temperature around CT for downward flow by $k-\omega$ model

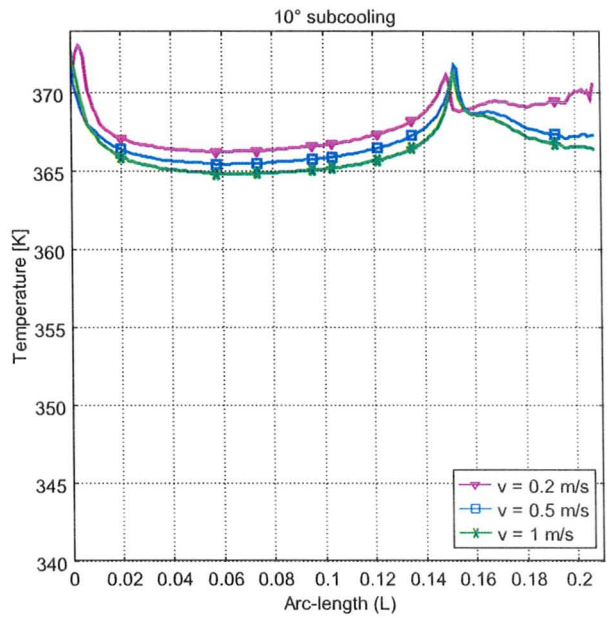

Figure 4.17: Local temperature for different velocities in upward flow by $k-\omega$ model

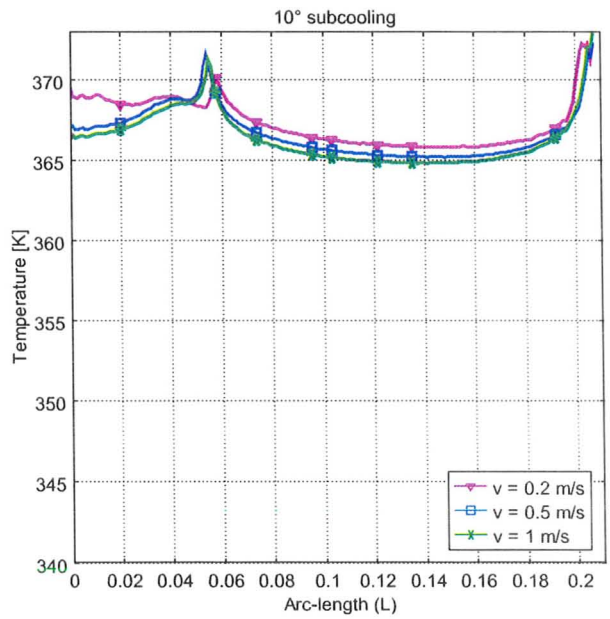

Figure 4.18: Local temperature for different velocities in downward flow, $k-\omega$ model

the overall temperature becomes higher. At very low velocity ($0.2m/s$), there is a relatively high temperature increase in the wake region for both upward and downward flows.

4.4 Comparison Between the Two Models

In general the variations in the hydrodynamic conditions of the flow around the cylinder can be described by the distribution of local pressure and local velocity. The boundary layer separation is due to internal friction within the boundary layer and is also related to the pressure and velocity distribution around the cylinder. Comparing Figures 4.3 and 4.13 which show the pressure and velocity variations around the cylinder obtained by $k-\epsilon$ and $k-\omega$ models respectively, indicates that the overall flow behavior is similar for both models. However, it can be seen that in $k-\omega$ predictions the separation point has moved forward and occurs at $L = 0.15$ while in the $k-\epsilon$ predictions it is at $L = 0.16$. In the $k-\omega$ predictions at the bottom of the cylinder due to the high temperature a non-zero velocity region is observed however it is very low. In addition in $k-\omega$ predictions, after the stagnation point in the bottom of the cylinder, the sharp increase in velocity starts with delay (at $L = 0.03$) comparing to the $k-\epsilon$ results (at $L = 0.02$).

Comparing Figures 4.6 and 4.15 which show the temperature distribution around the central CT obtained by $k-\epsilon$ and $k-\omega$ models respectively indicates some differences for the two models' predictions. In $k-\omega$ model the maximum temperature is at the forward stagnation point while in the $k-\epsilon$ model it is at the separation point on the cylinder. At low subcoolings the $k-\omega$ model predicts higher probability of

film boiling occurrence at the stagnation point in the front of the cylinder because not only the very low velocity results to accumulation of vapor bubbles but also the higher fluid temperature can lead to more bubble generation at this region. At high subcoolings the large temperature gradient will mitigate against significant vapor accumulation. This should also be noted that in $k-\epsilon$ results the local temperature variations around the cylinder are smaller which means that the change in the local temperature is smoother than the $k-\omega$ predictions. In the $k-\omega$ results there is a sharp change in the temperature at the forward stagnation point and at the separation point. This can be seen in Figure 4.19 and 4.20 as well. These figures show the temperature contours for $k-\epsilon$ and $k-\omega$ models respectively. This is clearly shown that each turbulence model shows different results.

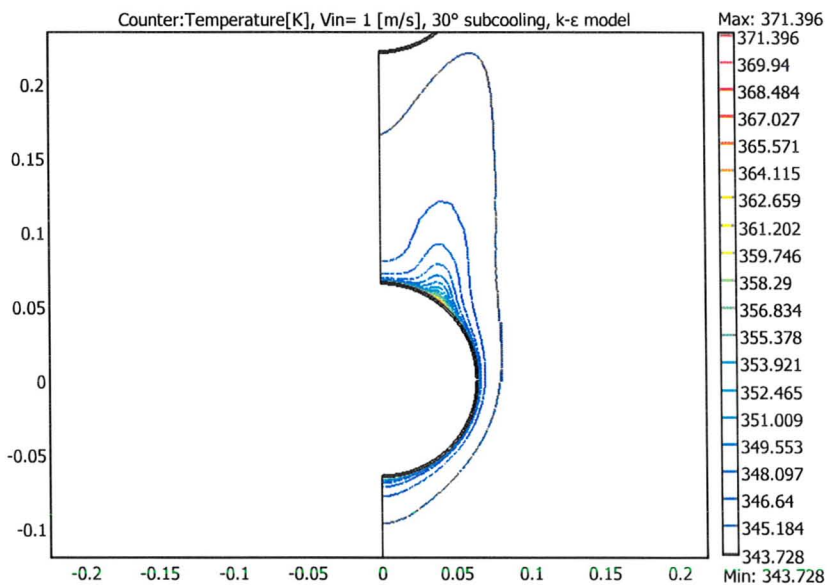

Figure 4.19: Temperature contours for $k-\epsilon$ model in upward flow

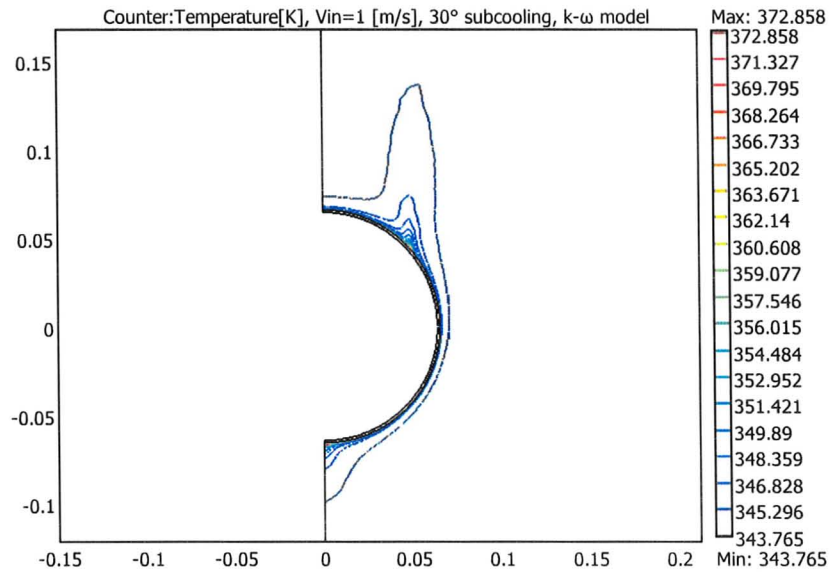

Figure 4.20: Temperature contours for $k-\omega$ model in upward flow

Comparing Figures 4.6 and 4.15 also indicates that in the $k-\omega$ predictions the temperature decreases sharply after the stagnation point from its highest value and it is near constant around the cylinder before the separation point at which the temperature again increases sharply. After the separation point, in the wake region again the temperature decreases due to the floe recirculation in the wake region. Although the same behavior was observed by the $k-\epsilon$ model but the temperature decreases smoothly from the stagnation point and again increases smoothly to reach to the separation point. In fact the high temperature regions predicted by $k-\epsilon$ model are not as localized as the one predicted by $k-\omega$ model.

Another important difference between the $k-\epsilon$ and $k-\omega$ models which can be seen from Figures 4.6 and 4.15 for upward flow is the significant differences in

temperature of the stagnation point in different subcoolings. The same behaviour is observed for downward flow in Figures 4.7 and 4.16. This can be explained by the differences in velocity distribution in the two models. Figure 4.21 (a) and (b) show the velocity streamlines for upward flow obtained by $k-\epsilon$ and $k-\omega$ model, respectively. For the $k-\epsilon$ model, the flow stream in region 2 is extended to the region 1 and it passes through the stagnation point on the bottom of the CT and therefore the fluid subcooling in region 2 affects the temperature of the stagnation point. Therefore the temperature at this point is reduced by increasing in subcooling (see Figures 4.6). Interestingly, for the $k-\omega$ model, the recirculation zone of the lower channel is extended to region 1 at the bottom of the central CT and the flow stream in region 2 does not affect significantly on that. Therefore the subcooled fluid from region 1 can not reach to the stagnation point and its subcooling does not affect the temperature at this region.

Figure 4.22 shows the heat transfer coefficient around the central CT at 20° subcooling and inlet velocity of $1m/s$ predicted by the two models. A minimum heat transfer coefficient occurs close to the top of the cylinder which is associated with separation, where local recirculation could restrict heat transfer from the surface. By moving further into the wake region the heat transfer coefficient increases as the turbulent wake allows heat to again be removed more effectively. It can be seen that in overall the $k-\epsilon$ model predicts a higher heat transfer coefficient around the cylinder compare to the $k-\omega$ model. It should be noted that a flow's capacity for convective heat transfer is affected by different factors one of which is levels of turbulence close to the heat transfer surface. Qualitatively, abnormally high levels of turbulence will

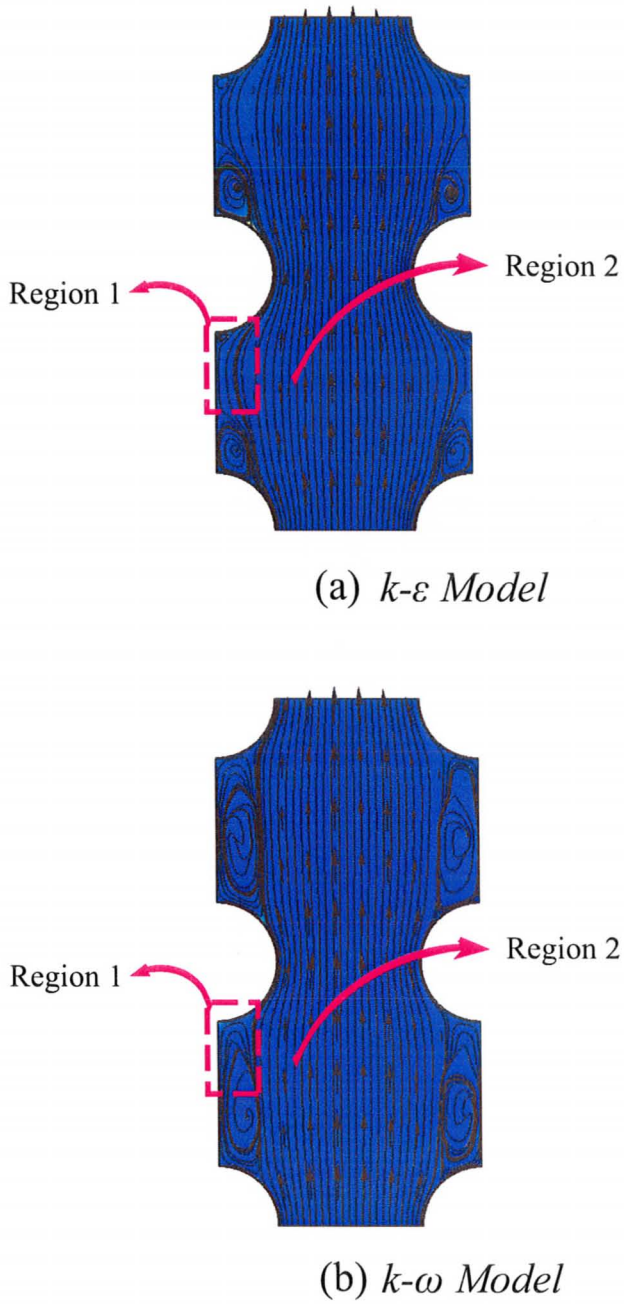

Figure 4.21: Velocity streamlines for upward flow, (a) $k-\epsilon$ and (b) $k-\omega$ model

result to abnormally high heat transfer due to turbulence affecting the flow's ability to transport heat away from the surface. Thus the $k-\epsilon$ turbulence model which over predicts levels of k close to the wall also over predicts the heat transfer from the wall. In addition, as we mentioned before, in this problem due to the importance of the curvature in the flow around the cylinder, $k-\omega$ is a better model than $k-\epsilon$.

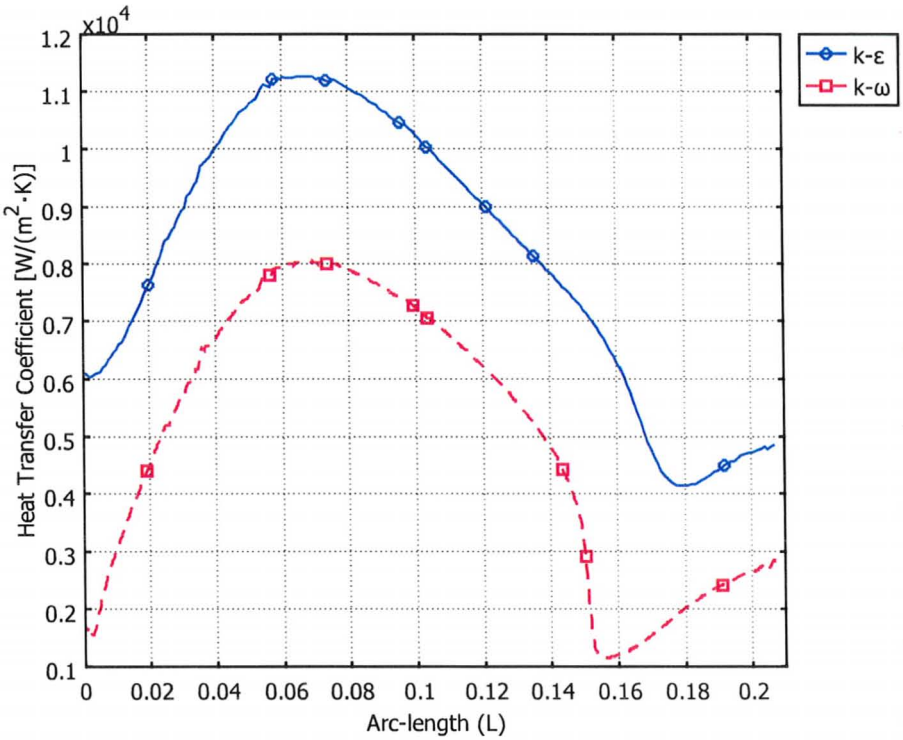

Figure 4.22: Local HTC around CT for upward flow, Vin= 1 [m/s]

Figures 4.23 and 4.24 show the temperature variations with time after $1s$ of heating for $k-\epsilon$ and $k-\omega$ models respectively. Minimum time step used in the model is $0.001s$. By further decreasing in time step, no significant change was observed. Heat

is implemented uniformly to the inner surface of the tube and increases exponentially by time. After $1s$ it reaches to its maximum value at which the maximum fluid temperature around the cylinder is near saturation. The maximum fluid temperature around the cylinder for the $k-\epsilon$ predictions is at the separation point while in the $k-\omega$ results it is at the stagnation point. In Figure 4.23 it can be seen that as time increases and more heat is added to the fluid, the temperature starts to rise sharply in the separation point and with a lower slope in the stagnation point. In Figure 4.24 we can see that in the $k-\omega$ predictions there is a sharp increase in temperature in the separation point and also a sharp rise in the stagnation point with an even higher slope.

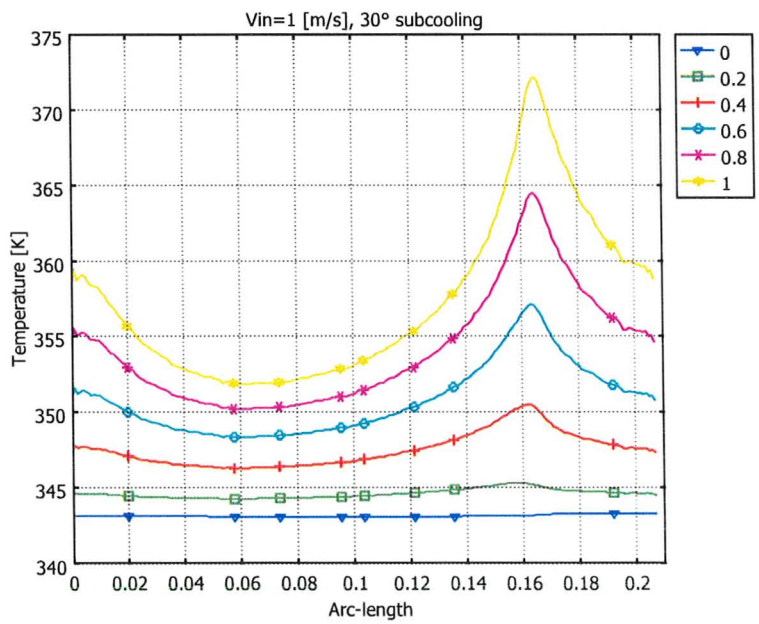

Figure 4.23: Temperature changes by time for upward flow obtained by $k-\epsilon$ model

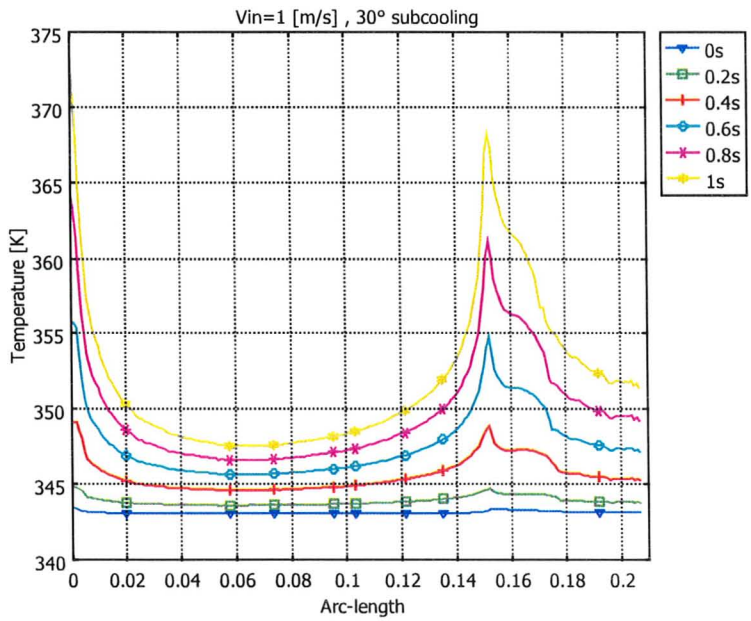

Figure 4.24: Temperature changes by time for upward flow obtained by $k-\omega$ model

4.5 Experimental data

In this study the Thermalhydraulic conditions around the CT surface after PT/CT contact and before boiling have been obtained in the two dimensional case and from these conditions the position at which film boiling occurs first has been predicted. In this section the predicted results will be compared with available experimental predictions and the differences will be discussed qualitatively.

Contact boiling experiments were performed at AECL Whiteshell Laboratories in Canada to investigate contact boiling heat transfer when a pressurized CANDU pressure tube deforms into contact with its calandria tube. The typical apparatus for these experiments is shown in Figure 4.25.

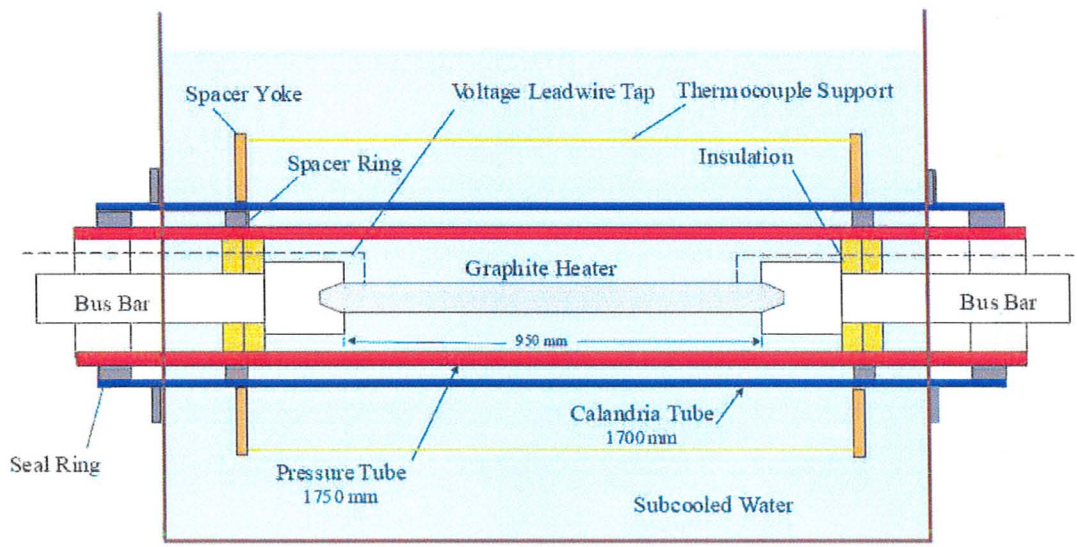

Figure 4.25: Experimental apparatus used in contact boiling tests (Fan, 2004)

The apparatus consists of a concentric pressure tube and calandria tube submerged in water. The nearly stagnant water is heated to a desired temperature by submerged steam lines. A graphite heater is located inside the test section at about the midpoint. The experiment is performed by pressurizing the inside of the pressure tube with Argon or Helium. Between the pressure tube and the calandria tube is purged with CO_2 at atmospheric pressure. The type of boiling in each test was reported both visually and by the calandria tube surface temperature which was monitored by thermocouple. Film boiling also forms oxide patches on the calandria tube surface. The oxidized area observed on the outside surface of calandria tube is shown in Figure 4.26 for a typical test. Wide patches of film boiling can be seen at angle of 180^o which is at the bottom of the cylinder in these tests.

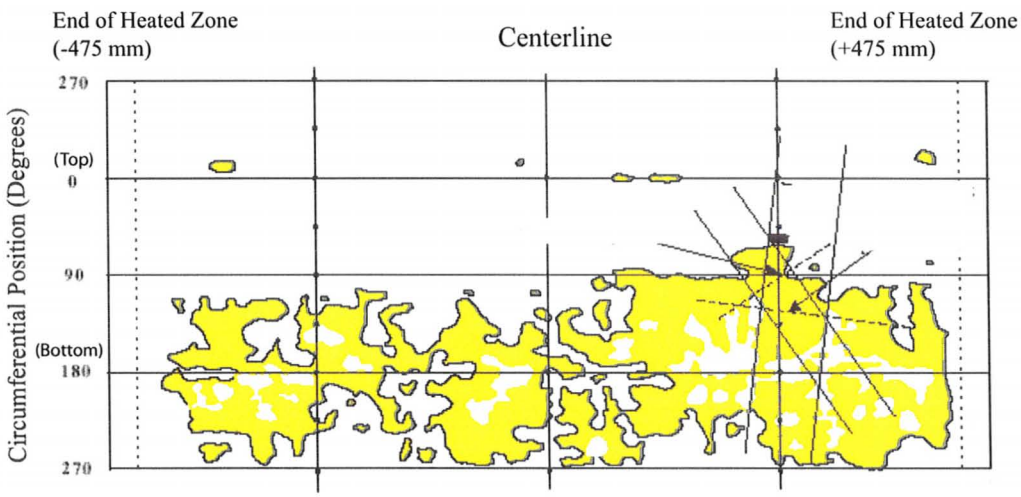

Figure 4.26: Areas of dryout on the CT for a typical test (Fan, 2004)

Similar experiments have been performed under COG (CANDU Owner Groups)

funding. In these experiments the film boiling patches on the CT surface were obtained mostly at the bottom of the cylinder when the internal pressure was around 4 MPa. At higher pressures around 8.5 MPa the results have shown more film boiling on the top of the CT. This can be explained by the fact that due to the internal natural convection inside the PT, the top of the PT was hotter than the bottom prior to contact and the top touched the calandria tube first. In this case because the internal pressure is high, the contact conductance between the PT and CT is also high and therefore the heat flux to the moderator is high enough to exceed the CHF and form a film boiling on the surface.

Since these experiments have been done for a single tube case, some simulations have been performed for a single CT using the same conditions described in previous chapters. The results for these simulations are described in this section of the thesis. In this model, the fluid enters the domain with 0.5 m/s velocity and at 5^o subcooling. The steady state problem in normal conditions has been solved first, in order to obtain consistent initial values for the transient case. The results for the transient case after 1s of heating due to the postulated PT/CT contact are shown below. Figure 4.27 shows the velocity streamlines for upward flow obtained by both $k-\epsilon$ and $k-\omega$ turbulent models. It can be seen that $k-\omega$ model predicts a larger wake in the downstream region. The same behavior was observed for downward flow showing in Figure 4.28. The effects of this difference between the two turbulent models have been discussed before in Figure 4.21 in the case of having tube banks. Figure 4.29 indicates the temperature distribution for the single channel simulation. For the upward flow, both turbulent models indicate a high temperature at the separation point. High

temperature at the top of the CT can lead to boiling. However the flow of fluid in the wake, causes spreading of the bubbles. As we explained in the previous sections, referring to Figure 4.30 for upward flow, one can conclude that at the stagnation region due to the very low velocity, it is more probable for bubble accumulation and film boiling to occur. These predictions by the model can be qualitatively verified by the above experiments.

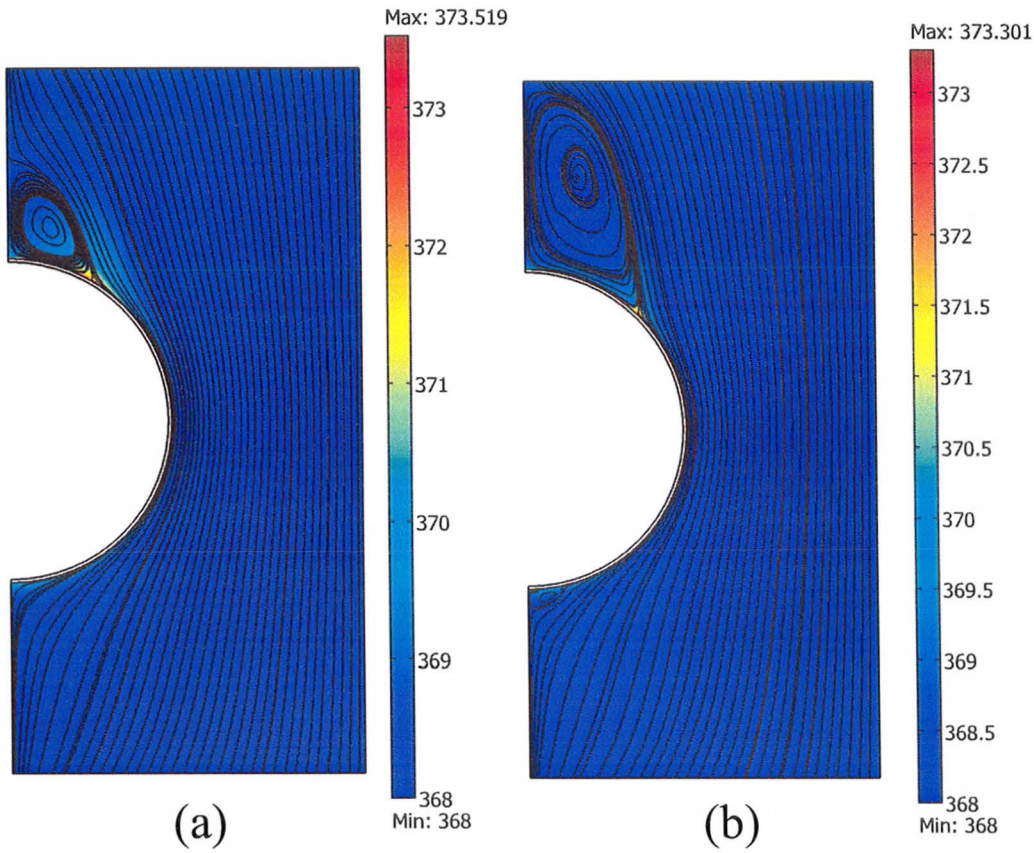

Figure 4.27: Velocity streamlines for the single CT, (a) $k-\epsilon$, (b) $k-\omega$ model

Another experimental work has been done by Thibault (1978) to investigate the boiling heat transfer around a horizontal cylinder and also in a tube bundle. In these

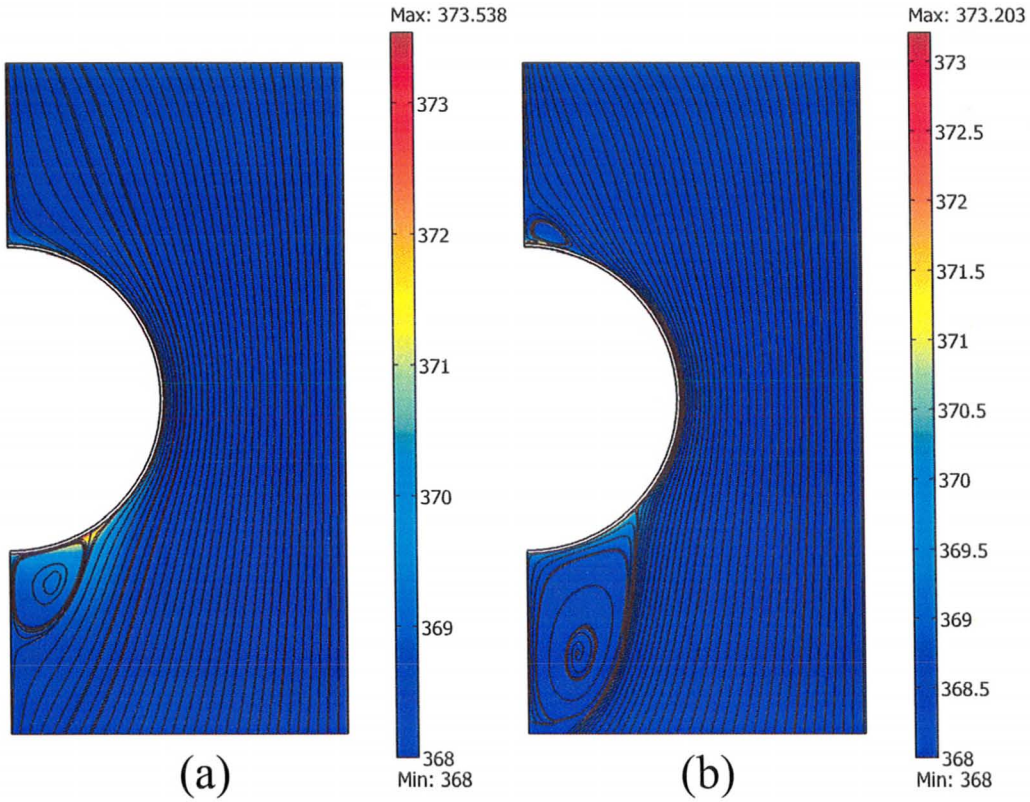

Figure 4.28: Velocity streamlines for the single CT, (a) $k-\epsilon$, (b) $k-\omega$ model

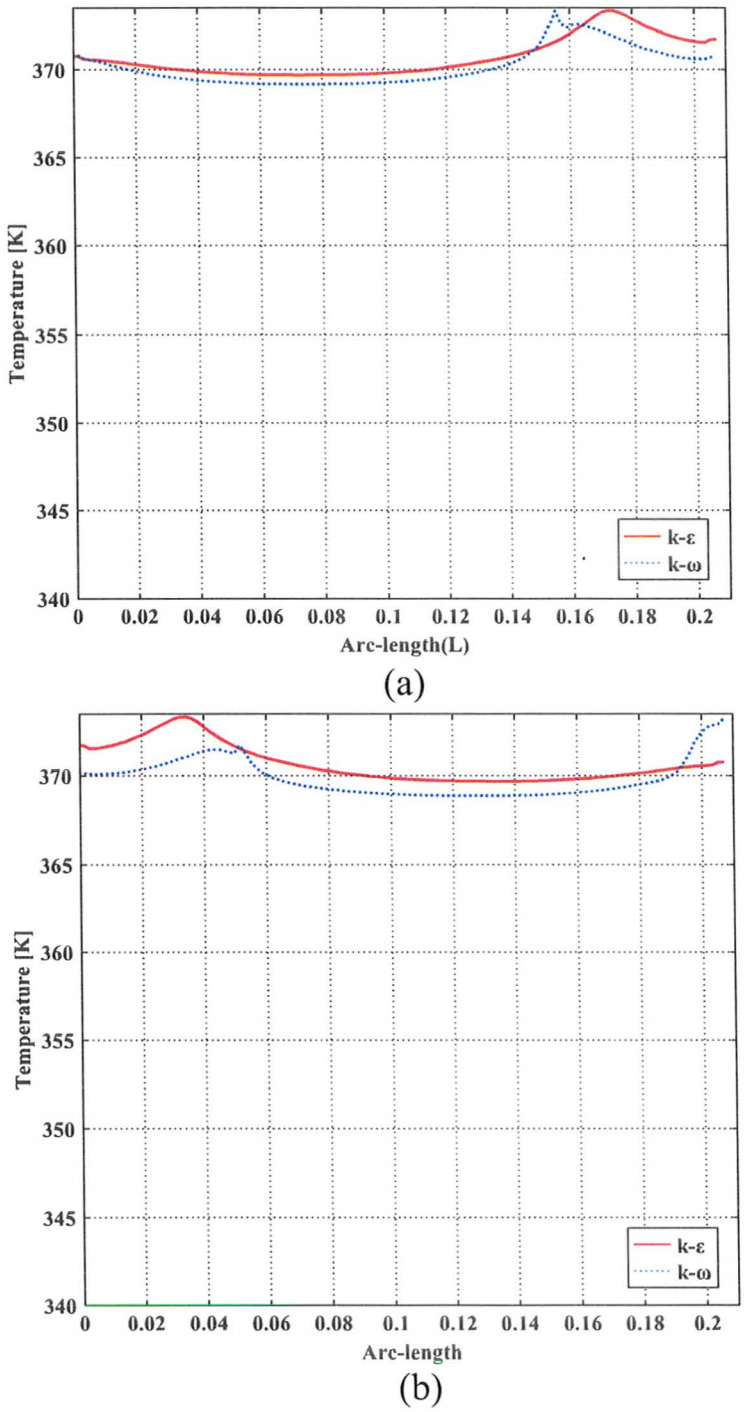

Figure 4.29: Local temperature for the single CT, (a) upward, (b) downward flow

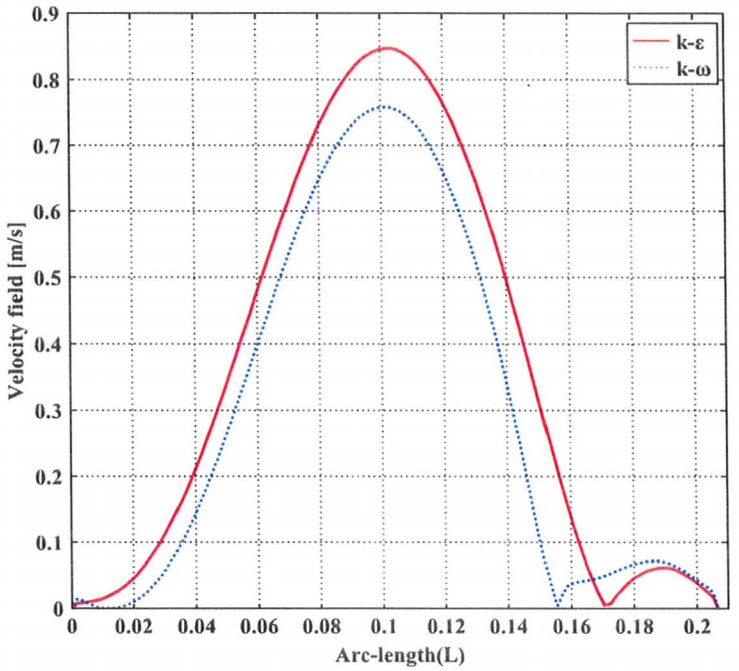

(a)

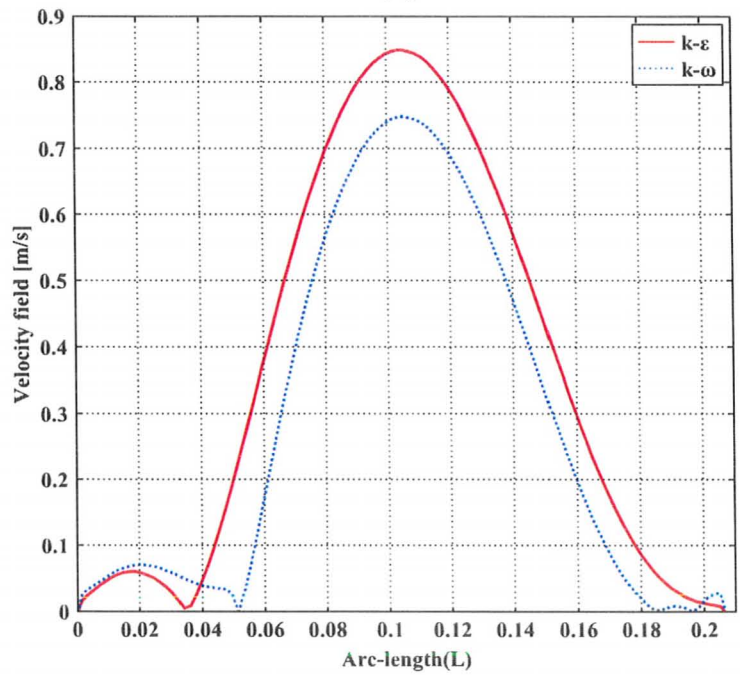

(b)

Figure 4.30: Local velocity for the single CT, (a) upward, (b) downward flow

experiments a copper cylinder 12.7 cm in diameter and 7.62 cm long equipped with a heat flux meter was heated to a high temperature and quenched in a pool of stagnant water at the desired level of subcooling to obtain the pool boiling heat transfer curve as a function of subcooling and location on the circumference. To simulate a long calandria tube the ends of the cylinder were insulated with transit disks which were used as a holder for the copper cylinder as well as to insulate it electrically from the metal frame and thermally from the surrounding liquid. Due to the small effect of the surface texture and material on the critical heat flux density, the author used a copper surface because of its high thermal conductivity, instead of a zirconium alloy. The copper cylinder was heated in an electrically heated oven to a temperature between 200^oC to 300^oC depending on the level of subcooling. Copper oxidation was minimized by a continuous flow of Nitrogen to the oven. The copper cylinder was removed and quenched in the tank of water at the desired level of subcooling. One boiling curve was obtained from each quenching experiment. In addition, the boiling curves were determined at seven different angles uniformly distributed from top to bottom of the cylinder. In the second part of the experiments the author obtained the boiling curve on a 12.7 cm diameter tube located in a bank of similar tubes undergoing the same boiling phenomena.

The author found that the maximum critical heat flux occurs at the top of the cylinder and the minimum critical heat flux occurs at an angle of 30^o from the top of the cylinder for saturated boiling. High speed motion pictures revealed intermittent separation of the upflowing vapor-liquid boundary layer at about 30^o and therefore

the author concluded that the minimum value for CHF at this point arose from external hydrodynamic effects rather than the internal conduction effects. This minimum CHF at 30^o disappeared when the liquid was subcooled 10^oC or more. The CHF at other angles were lower than that at the top. The author concluded that the variations in CHF around the cylinder is directly related to the fluid mechanical behavior of the liquid-vapor around the cylinder. Again it should also be noted that all the experiments were done in pool boiling conditions and the forced convection effects are not considered which can change the distribution of heat flux around the cylinder. In addition by increasing the subcooling the natural convection effects becomes more important. As the upward liquid flow proceeds around the cylinder, the local subcooling decreases. Forming and collapsing of vapor bubbles also play an important role in affecting local CHF.

Obtained CHF densities by Thibault (1978) for 10^oC subcooling is shown in the table below and also in Figure 4.31. The lowest CHF value at the bottom of the cylinder indicates the greater tendency for film boiling to occur at this region. Therefore the results obtained by our model which shows the potential of film boiling to occur at the top or at the bottom of the CT are in agreement with Thibault (1978)'s experiments.

angle	0	30	60	90	120	150	180
CHF	168.3	166.7	135.9	163.1	138.9	132.2	125.1

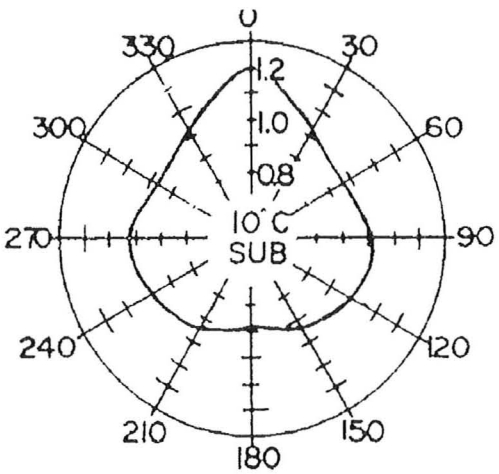

Figure 4.31: Local CHF around a cylinder for 10^{o}C subcooling (Thibault, 1978)

Chapter 5

Conclusions and Future Work

In some LOCAs for a particular break size and location referred to as critical break LOCA, the coolant flow through a portion of the reactor core stagnates before the emergency coolant injection restores circulation or it fails to operate. In this situation, fuel cooling becomes severely degraded due to rapid flow reduction in the affected flow pass of the heat transport system. This can result in pressure tube experiencing significant heatup while coolant pressure is still high, thereby causing uniform thermal creep strain (ballooning) of the PT into contact with its CT. Contact of the hot PT with the CT leads to rapid redistribution of stored heat from the PT to CT and a large spike in heat flux from the CT to the moderator fluid. For lower subcooling conditions of the moderator, dryout of the CT can occur. The focus of this research was to establish a Computational Fluid Dynamics (CFD) model for predicting the moderator flow field and temperature distribution around one single channel to investigate the potential of dryout occurrence on the CT surface following a PT/CT contact.

In this thesis, flow field and temperature distribution around the calandria tube of a CANDU reactor fuel channel following PT/CT contact have been predicted.

Buoyancy forces due to density variations has been taken into account and the fluid is considered to be single phase. Velocity, pressure and temperature profile around the cylinder are indicated. Two different turbulent models $k-\epsilon$ and $k-\omega$ are used separately to predict the fluid turbulence and the obtained results are compared together. The model clearly indicates the wake region behind the cylinder. It also shows the stagnation region in front of the cylinder at which the velocity is zero and it can be concluded that the stagnated flow can result to accumulation of the bubbles and consequent stable vapor film generation at this region. Some major differences were observed in the predictions of the two turbulence models. $k-\omega$ model predicts the highest temperature at the stagnation point in front of the cylinder while $k-\epsilon$ model predicts the highest temperature at the separation point on the cylinder. In the $k-\epsilon$ predictions, the separation point at which the boundary layer detaches from the surface occurs at $\theta = 137°$ while in the $k-\omega$ it has moved forward and occurs at $\theta = 129°$ for upward flow condition.

The predicted local temperature variations with subcooling illustrates a greater tendency for vapor film to extend around the CT surface at low subcooling for both $k-\omega$ and $k-\epsilon$ models. This shows the importance of moderator subcooling in preventing the vapor film to extend on the CT surface. In the $k-\omega$ predictions, the temperature decreases sharply from its highest value after the stagnation point and it is almost constant around the cylinder before the separation point at which the temperature again increases sharply. After the separation point, in the wake region again the temperature decreases due to the flow recirculation in the wake region. Although the same behaviour was observed by the $k-\epsilon$ model but the temperature

decreases smoothly from the stagnation point and again increases smoothly to reach to the separation point. In fact the high temperature regions predicted by $k-\epsilon$ model are not as localized as the one predicted by $k-\omega$ model. The $k-\epsilon$ model predicts a higher heat transfer coefficient around the cylinder compare to the $k-\omega$ model. For both models a minimum heat transfer coefficient occurs close to the top of the cylinder which is associated with separation, where local recirculation could restrict heat transfer from the surface. By moving further into the wake region the heat transfer coefficient increases as the turbulent wake allows heat to again be removed more effectively. The $k-\epsilon$ turbulence model overpredicts levels of k close to the wall and therefore overpredicts the heat transfer from the wall. In addition, in this problem due to the importance of the curvature in the flow around the cylinder, $k-\omega$ is a better model than $k-\epsilon$.

For future works, further simulations need to be performed to investigate the behavior of bubble generation and thermal-hydraulic conditions in order to demonstrate the film boiling phenomena. In fact the modelling should be extended to include localized two-phase conditions near the CT wall. Using the thermalhydraulic conditions predicted from CFD analysis, a mechanistic model needs to be developed for predicting CHF on the CT and then extend it to prediction of quenching of drypatches.

Bibliography

Austman, G., Szymanski, J., Garceau, M., and Midvidy, W. (1985). Measuring moderator temperature in a candu reactor. 6^{th} *Annual Conference of CNS, Ottawa, Canada.*

Austman, G. Szymanski, J. M. W. (1982). Modcir: A three-dimensional transient code used in thermal-hydraulic analysis of candu power reactor. *Proceedings of the 10th IMACS World Congress on Systems Simulation and Scientific Computatio, Montreal, Quebec.*

Burmeister, L. C. (1993). *Convective Heat Transfer.* John Wiley and Sons, INC., New York, NY.

Choo, C.K. Austman, G. C. Y. M. W. (1980). Numerical simulation of moderator circulation in the calandria vessel. *Proceedings of the 7th Simulation Symposium on Reactor Dynamics and Plant Control, Montreal, Quebec.*

COMSOL (2008). *COMSOL Chemical Engineering Module User's Guide.*

Fan, H.Z Bilanivic, Z. (2004). Use of cathena to model calandria-tube/moderator

heat transfer after pressure tube/calandria tube ballooning contact. *CNS 6^{th} International Conference on Simulation Methods in Nuclear Engineering, Montreal, Quebec, Canada.*

Gillespie, G. (1981). An experimental investigation of heat transfer from a reactor fuel channel to surrounding water. 2^{nd} *Annual Conference of the Canadian Nuclear Society*, pages 157–163.

Holmgren, M. (2007). *XSteam for MATLAB, Thermodynamic Properties of Water and Steam.* http://www.mathworks.com.

Huget, R., Szymanski, J., and Midvidy, W. (1989). Status of physical and numerical modelling of candu moderator circulation. *Proceedings of* 10^{th} *Annual Conference of Canadian Nuclear Society, Ottawa, Canada.*

Huget, R., Szymanski, J., and Midvidy, W. (1990). Experimental and numerical modelling of combined forced and free convection in a complex geometry with internal heat generation. *Proceedings of* 9^{th} *International Heat Transfer Conference, Jeursalem, Israel.*

Incropera, F. DeWitt, D. (1990). *Introduction to Heat Transfer.*

Jones, W. and Launder, B. (1972). The prediction of laminarization with a two-equation model of turbulence. *Int.J. Heat and Mass Transfer*, **15**, 301–314.

Kays, W. (1994). Turbulent prandtl number. where are we? *Journal of Heat Transfer*, **116**, 284–295.

Khartabil, H., Inch, W., Szymanski, J., Novog, D., Tavasoli, V., and Mackinnon, J.

(2000). Three dimentional moderator circulation experimental program for validation of cfd code modturc-clas. 21^{st} *CNS Nuclear Simulation Symposium, Ottawa, Canada.*

Kim, M., Yu, S. O., and Kim, H. J. (2005). Analysis on fluid flow and heat transfer inside calandria vessel of candu-6 using cfd. *Nuclear Engineering and Design*, **236**(11), 1155–1164.

Launder, B. and Spalding, D. (1972). *Mathematical model of turbulence.* Academic Press., London.

Luxat, J. (2007). Thermalhydraulic aspects of progression to severe accidents in candu reactors. 12^{th} *International Topical Meeting on Nuclear Reactor Thermalhydraulics (NURETH-12), Pennsylvania, U.S.A.*

MatPRO (1993). A library of materials properties for light-water-reactor accident analysis. *SCDAP/RELAP5/MOD3.1 Code Manual*, **IV**.

Menter, F. (1994). Two-equation eddy-viscosity turbulence models for engineering applications. *AIAA journal*, **32**(8), 1598–1605.

Pope, S. B. (2000). *Turbulent Flows.* Cambridge University Press, Cambridge, UK.

Reynolds, O. (1895). On the dynamical theory of incompressible viscous fluids and the determination of the criterion. *Philosophical Transactions of the Royal Society of London, Series A*, **186**, 123.

Schlichting, H. Gersten, K. (2000). *Boundary Layer Theory.* Springer.

Szymanski, J., Garceau, K., and Midvidy, W. (1983). Numerical modeling of three-dimentional turbulent moderator flow in calandria. *Canadian Nuclear Society/American Nuclear Society International Conference on Numerical Methods in Nuclear Engineering*, **2**, 970–984.

Thibault, J. (1978). *Boiling Heat Transfer Around a Horizontal Cylinder and in Tube Bundles*. PhD. Thesis, McMaster university, Hamilton, Ontario.

Von Karman, T. (1930). Mechanische ahnlichkeit und turbulenz. *Third Int. Congr. Applied Mechanics, Stockholms*, pages 85–105.

Wilcox, D. (1998). *Turbulence Modeling for CFD*. DCW Industries Inc.

Yoon, C., Rhee, B. W., KIM, H. T., PARK, J. H., and Min, B. J. (2006). Moderator analysis of wolsong units 2/3/4 for the 35% reactor inleat header break with a loss of emergency core cooling system. *Journal of Nuclear Science and Technology*, **43**, 505–513.

Zienkiewicz, O.C. Taylor, R. N. P. (2005). *The Finite Element Method for Fluid Dynamics*. Elsevier Butterworth-Heinemann, Oxford.

Zukauskas, A. Ziugzda, J. (1985). *Heat Transfer of a Cylinder in Crossflow*. Hemishere Pub, Washington; New York.

Zukauskas, A. Ulinskas, R. (1988). *Heat Transfer in tube banks in Crossflow*. Hemishere Pub, Washington; New York.